



# Enabling coherent BaZrO<sub>3</sub> nanorods/YBa<sub>2</sub>Cu<sub>3</sub>O<sub>7-x</sub> interface through dynamic lattice enlargement in vertical epitaxy of BaZrO<sub>3</sub>/YBa<sub>2</sub>Cu<sub>3</sub>O<sub>7-x</sub> nanocomposites

Judy Z Wu<sup>1,\*</sup> , Victor Ogunjimi<sup>1,\*</sup> , Mary Ann Sebastian<sup>2,3</sup>, Di Zhang<sup>4</sup>, Jie Jian<sup>4</sup>, Jijie Huang<sup>4</sup>, Yifan Zhang<sup>4</sup>, Bibek Gautam<sup>1</sup> , Timothy Haugan<sup>2,3</sup> and Haiyan Wang<sup>4</sup> 

<sup>1</sup> Department of Physics and Astronomy, University of Kansas, Lawrence, KS 66045, United States of America

<sup>2</sup> University of Dayton Research Institute, Dayton, OH 45469, United States of America

<sup>3</sup> U.S. Air Force Research Laboratory, Aerospace Systems Directorate, WPAFB, OH 45433, United States of America

<sup>4</sup> School of Materials Engineering, Purdue University, West Lafayette, IN 47907, United States of America

E-mail: [jwu@ku.edu](mailto:jwu@ku.edu) and [victorogunjimi@ku.edu](mailto:victorogunjimi@ku.edu)

Received 28 August 2021, revised 6 January 2022

Accepted for publication 13 January 2022

Published 4 February 2022



## Abstract

One-dimensional *c*-axis-aligned BaZrO<sub>3</sub> (BZO) nanorods are regarded as strong one-dimensional artificial pinning centers (1D-APCs) in BZO-doped YBa<sub>2</sub>Cu<sub>3</sub>O<sub>7-x</sub> (BZO/YBCO) nanocomposite films. However, a microstructure analysis has revealed a defective, oxygen-deficient YBCO column around the BZO 1D-APCs due to the large lattice mismatch of ~7.7% between the BZO (3a = 1.26 nm) and YBCO (c = 1.17 nm), which has been blamed for the reduced pinning efficiency of BZO 1D-APCs. Herein, we report a dynamic lattice enlargement approach on the tensile strained YBCO lattice during the BZO 1D-APCs growth to induce *c*-axis elongation of the YBCO lattice up to 1.26 nm near the BZO 1D-APC/YBCO interface via Ca/Cu substitution on single Cu-O planes of YBCO, which prevents the interfacial defect formation by reducing the BZO/YBCO lattice mismatch to ~1.4%. Specifically, this is achieved by inserting thin Ca<sub>0.3</sub>Y<sub>0.7</sub>Ba<sub>2</sub>Cu<sub>3</sub>O<sub>7-x</sub> (CaY-123) spacers as the Ca reservoir in 2–6 vol.% BZO/YBCO nanocomposite multilayer (ML) films. A defect-free, coherent BZO 1D-APC/YBCO interface is confirmed in transmission electron microscopy and elemental distribution analyses. Excitingly, up to five-fold enhancement of *J<sub>c</sub>* (*B*) at magnetic field *B* = 9.0 T//*c*-axis and 65 K–77 K was obtained in the ML samples as compared to their BZO/YBCO single-layer (SL) counterpart's. This has led to a record high pinning force density *F<sub>p</sub>* together with significantly enhanced *B<sub>max</sub>* at which *F<sub>p</sub>* reaches its maximum value *F<sub>p,max</sub>* for BZO 1D-APCs at *B*//*c*-axis. At 65 K, the *F<sub>p,max</sub>* ~158 GN m<sup>-3</sup> and *B<sub>max</sub>* ~ 8.0 T for the 6% BZO/YBCO ML samples represent a significant enhancement over *F<sub>p,max</sub>* ~ 36.1 GN m<sup>-3</sup> and *B<sub>max</sub>* ~ 5.0 T for the 6% BZO/YBCO SL counterparts. This result

\* Authors to whom any correspondence should be addressed.

not only illustrates the critical importance of a coherent BZO 1D-APC/YBCO interface in the pinning efficiency, but also provides a facile scheme to achieve such an interface to restore the pristine pinning efficiency of the BZO 1D-APCs.

Supplementary material for this article is available [online](#)

**Keywords:** YBCO nanocomposites, 1D artificial pinning center, vortex pinning efficiency, vertical epitaxy, coherent interface, dynamic lattice enlargement

(Some figures may appear in colour only in the online journal)

## 1. Introduction

Pinning of quantized magnetic vortices using nanoscale artificial pinning centers (APCs) can lead to significantly enhanced critical current density ( $J_c$ ) in high temperature superconductors, such as *c*-axis oriented epitaxial  $\text{YBa}_2\text{Cu}_3\text{O}_{7-x}$  (YBCO) thin films and coated conductors [1–3]. Among others, self-assembled *c*-axis aligned one-dimensional (1D) APCs of various oxides, such as  $\text{BaZrO}_3$  (BZO) [4–10],  $\text{BaSnO}_3$  [11, 12],  $\text{BaHfO}_3$  (BHO) [13–19], and double perovskites such as  $\text{YBa}_2(\text{Nb/Ta})\text{O}_6$  and other rare-earth tantalates, niobates and hafnates [20–24] have been reported to provide strong correlated pinning of the magnetic vortices, leading to enhanced critical current density  $J_c$  when the applied magnetic field  $B$  is parallel to the one-dimensional artificial pinning centers (1D-APCs).

It should be noted that self-assembly of the impurity 1D-APCs in the YBCO matrix via vertical epitaxy is driven by a strain field that originates from the 1D-APC/YBCO interface due to their lattice mismatch at the interface (in the direction of the *c*-axis of YBCO perpendicular to the film), which is similar to the case of vertically self-organized InAs quantum box islands on GaAs (100) surface [25, 26]. Xie *et al* developed the first analytical description of the correlated island formation under strain, which revealed the critical role of the interface lattice mismatch induced strain field as the driving force for such vertical self-organized growth [27]. For superconductor nanocomposite films with APCs, Shi *et al* further analyzed the strain fields with considerations of three interfaces involved, namely interfaces of APC/YBCO, YBCO/substrate and APC/substrate, in order to obtain a quantitative understanding, through a comparison with experiment, the effect of strain field on the morphology of APCs, and the orientation and diameter of the 1D-APCs [28–30]. Specifically in the case of the BZO 1D-APC/YBCO nanocomposites, the large lattice constant of the BZO results in a positive lattice mismatch of  $\sim 7.7\%$  at the BZO 1D-APC/YBCO interface and hence a tensile strain on the *c*-axis of YBCO. The strained 1D-APC/YBCO interface is common in the reported 1D-APC/YBCO nanocomposites due to the APC/YBCO lattice mismatch including BHO 1D-APCs at 6.9%, BSO at 5.7% and  $\text{YBa}_2(\text{Nb/Ta})\text{O}_6$  at 2.9%.

However, the large strain beyond the accommodation limit of the two constituent, dissimilar ceramic materials across the epitaxial 1D APC/YBCO interface, such as BZO/YBCO, has been found to cause formation of defects at the interface. As

shown in a high-resolution electron microscopy study of the BZO/YBCO interface, a cylindrical YBCO shell with a thickness of a few nm around the BZO 1D-APCs has been found containing a large concentration of defects such as dislocations with much reduced superconductivity due to oxygen deficiency [31, 32]. Since the specific pinning force (or pinning force per unit length) of the BZO 1D-APCs is proportional to the radial derivative of the pinning energy at the BZO/YBCO interface [33], Cantoni *et al* indicated that the reduced superconductivity in this YBCO shell at the BZO/YBCO interface is expected to degrade the pinning efficiency of the BZO 1D-APCs [31]. In contrast, Horide *et al* argued that this defective YBCO shell would not generate significant degradation on pinning efficiency of BZO 1D-APCs due to the electron screen effect and the small layer thickness  $\sim 3$  YBCO unit cells  $<$  coherence length [32]. Therefore, experimental investigation of the effect of the BZO/YBCO interface on pinning efficiency of BZO 1D-APCs is important and urgent. In a comparative study of the pinning efficiency of BZO and BHO 1D-APCs of similar morphology (5–6 nm in diameter) and doping range of 2–6 vol.% in YBCO, a considerably higher pinning force density ( $F_p$ ) was observed on BHO 1D-APCs at lower BHO doping up to 4 vol.%, which was attributed to a less defective or more coherent BHO/YBCO interface than the BZO/YBCO case [34]. However, the large BHO/YBCO lattice mismatch of 6.7%, which is comparable to the 7.7% BZO/YBCO lattice mismatch, resulted in a highly strained BHO/YBCO lattice due to strain field overlap. This has an immediate impact that the 6 vol.% BHO/YBCO has a very low transition temperature ( $T_c$ ) of 78.5 K and unmeasurable or very low  $J_c$  at 77 K–65 K. Importantly, this result indicates that the benefit of a coherent APC/YBCO interface on pinning enhancement can be outweighed by the detrimental strain field overlap on YBCO lattice due to degraded superconductivity. This means that new approaches are needed to enable: (a) a coherent 1D-APC/YBCO interface for high APC pinning efficiency and (b) low strain field overlap on the APC/YBCO lattice for negligible (or low) degradation of the superconductivity on YBCO lattice especially at high APC doping.

Herein, we report a multilayer approach to achieve a coherent BZO/YBCO interface by enlarging the *c*-axis lattice constant of YBCO via formation of planar defects on YBCO lattice through partial replacement of smaller Cu with larger (by 30% in dimension) Ca cations on the Cu-O planes. This Ca/Cu replacement is driven by the tensile strain at the BZO 1D-APC/YBCO interface and would be energetically

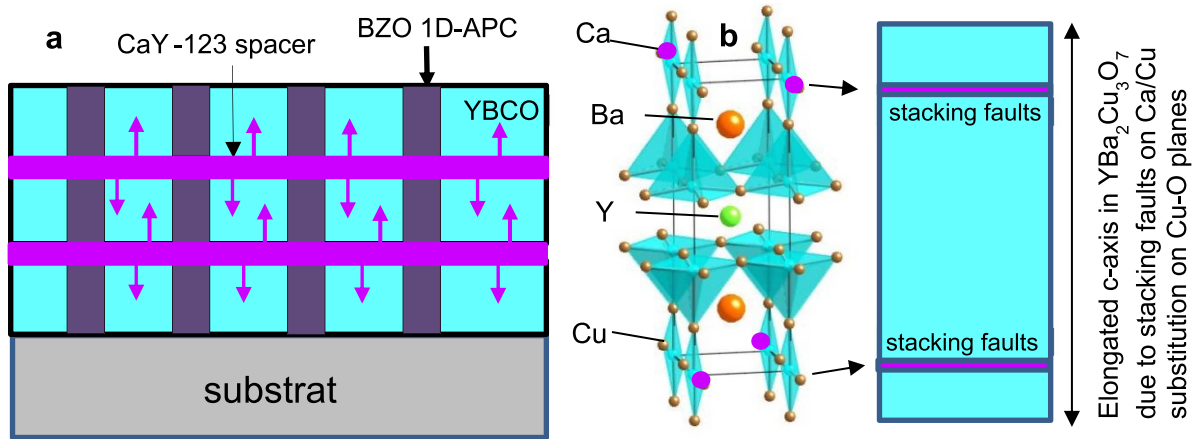


**Figure 1.** Schematic of multilayers consisting of three BZO (brown) doped YBCO (blue) layers stacking alternatively with two CaY-123 spacers (purple) layers. The Ca diffusion from the spacers to YBCO is illustrated by the purple arrows; and (b)  $c$ -axis enlargement in a  $\text{YBa}_2\text{Cu}_3\text{O}_7$  unit cell as a consequence of the stacking faults formed due to partial Ca/Cu substitution on the Cu-O planes.

preferred to reduce the strain on the YBCO lattice to minimize degradation of superconductivity especially at high BZO doping. In a recent work on 2 vol.% BZO 1D-APC/YBCO multilayers by inserting two thin  $\text{Ca}_{0.3}\text{Y}_{0.7}\text{Ba}_2\text{Cu}_3\text{O}_{7-x}$  (CaY-123) spacers to provide a controllable Ca diffusion, a partial Ca/Cu replacement on the Cu-O planes and the consequent elongation of the  $c$ -axis of YBCO up to  $\sim 1.26$  nm has been confirmed, which led to  $\sim 70\%$  enhancement of  $F_p$  at 65 K as compared to the [35]. In this manuscript, we carry out a systematic study of this dynamic lattice enlargement process on 2–6 vol.% BZO-doped YBCO nanocomposite multilayer films (2%–6% BZO/YBCO ML). Remarkably, we show that the YBCO  $c$ -axis lattice enlargement leads to a highly coherent BZO 1D-APC/YBCO interface due to the significantly reduced lattice mismatch at the interface from 7.7% to 1.4% in the BZO/YBCO ML samples. In comparison with the reference 2%–6% BZO/YBCO single-layer (2%–6% BZO/YBCO SL) films, remarkably enhanced  $J_c(B)$  at high magnetic fields up to 9.0 T has been obtained. At 9.0 T, a five folds enhancement of the  $J_c$  is obtained in the temperature range of 65 K–77 K on 6% BZO/YBCO ML samples.

## 2. Experiment

### 2.1. Sample fabrication

Two sets of the 2–6 vol.% BZO doped YBCO nanocomposite films were deposited on (100)  $\text{SrTiO}_3$  (STO) single crystal substrates using pulsed laser deposition (PLD) [10, 36, 37]. One set consisting of SL YBCO films doped with different concentrations of BZO in the range of 2–6 vol.% (2%–6% BZO/YBCO-SL) were made as reference samples for extraction of the Ca/Cu replacement effect. The other set would be otherwise the same except with two additional Ca-containing spacer layers inserted in each BZO doped YBCO nanocomposite film. Specifically,  $\text{Ca}_{0.3}\text{Y}_{0.7}\text{Ba}_2\text{Cu}_3\text{O}_{7-x}$  (CaY-123) was used for the Ca-containing spacers. These samples have a multilayer structure with three 45–50 nm thick BZO doped

YBCO layers separated by two CaY-123 spacers (2%–6% BZO/YBCO ML) as illustrated schematically in figure 1(a). The amount of the Ca was controlled by varying the thickness of the CaY-123 layer ( $t_{\text{spacer}}$ ) in the range of 5–15 nm and the Ca diffusion time, by the PLD repetition rate  $R_{\text{spacer}}$  in the range of 1–4 Hz. The total thickness of samples in both sets is  $\sim 160$ – $180$  nm. All ML and SL samples were deposited at the substrate temperature of  $\sim 825$  °C in 300 mTorr oxygen ( $\text{O}_2$ ) environment optimized to the 2%–6% SL samples in our previous works [10]. About 8 Hz repetition rate was used for PLD growth of the BZO doped YBCO layers in both sets of the samples. For convenience of the discussion on the effect of the  $t_{\text{spacer}}$  and  $R_{\text{spacer}}$ , the samples in the second set are labeled as: 2%–6% ML ( $t_{\text{spacer}} - R_{\text{spacer}}$ ). After the deposition, the samples were annealed for about 30 min dwell time at 500 °C in one atmosphere  $\text{O}_2$  pressure.

### 2.2. Sample characterization

The film thicknesses were measured using a Tencor P-16 profilometer. For electrical transport measurement, Ag contact pads were sputtered on the samples through a shadow mask. The samples were then patterned using standard photolithography (Leica) to create two microbridges of length  $\sim 500$   $\mu\text{m}$  and width of 20 and 40  $\mu\text{m}$  respectively. The details of the patterning and sample wiring for the transport measurement can be found in our previous works [20, 38]. The samples were mounted on a oxygen-free Cu stage using Ag paste and resistance–temperature ( $R$ – $T$ ) and current–voltage ( $I$ – $V$ ) characteristic curves were measured as function of temperature  $T$  (65 K–77 K) and the magnetic field  $B$  (up to 9.0 T) applied in the  $c$ -axis of the BZO/YBCO films in a Quantum Design Ever-Cool II Physical Property Measurement System. To minimize the heating at high currents, a pulsed current source (Keithley 2430 1KW Pulse Source Meter) was adopted with the pulse width of  $\sim 500$  ms for the  $I$ – $V$  curves.  $J_c$  was determined by applying  $1 \mu\text{V cm}^{-1}$  standard criterion [38–40]. The  $N$  values were extracted through fitting the measured  $I$ – $V$  curves using

the formula of  $V \propto I^N$  [41]. X-ray diffraction (XRD)  $\theta - 2\theta$  patterns were taken using a Bruker D8 Discover diffractometer to determine the  $c$ -axis lattice constant of the films. Transmission electron microscopy (TEM) and scanning transmission electron microscopy (STEM) under a high angle annular dark field mode (HAADF) were taken using a Thermo Fisher Scientific TALOS F200X TEM system with a point-to-point resolution of 1.6 Å. High-resolution STEM (HRSTEM) images were taken on a Thermo Fisher Scientific Themis-Z TEM system that is a new generation aberration-corrected electron microscope with the STEM resolution as small as 63 pm at acceleration voltage of 300 kV with combined correctors. A Digital Micrograph plug-in (DM 1.8.3 package, HRTEM Research Inc.) was employed for the geometric phase analysis (GPA). The cross-sectional TEM samples were prepared using a standard procedure, including manual grinding, polishing, dimpling and a final ion-milling step (PIPS 691 precision ion polishing system, Gatan Inc.).

### 3. Results and discussions

Figure 1(a) illustrates schematically the cross-sectional view of the 2%–6% BZO/YBCO ML samples, consisting of three BZO (brown)/YBCO (blue) layers stacking alternately with the two CaY-123 spacers (purple). The selection of the BZO/YBCO as the first layer of the BZO/YBCO ML samples would allow the same morphology and the concentration of the BZO 1D-APCs to form in the BZO/YBCO ML samples as in their BZO/YBCO SL counterparts. The CaY-123 spacers serve as Ca reservoir to allow Ca ions diffuse into the BZO/YBCO layer. The purple arrows in figure 1(a) illustrate schematically the Ca diffusion from spacers into YBCO for the possible Ca/Cu substitution on the Cu-O planes that leads to formation of stacking faults and hence elongation of the  $c$ -axis (figure 1(b)). The amount of the Ca diffusion can be controlled by varying the thickness of the CaY-123 spacers  $t_{\text{spacer}}$ , and the PLD repetition rate  $R_{\text{spacer}}$  respectively. It should be noted that the CaY-123 spacer may truncate the BZO 1D-APCs into segments with reduced pinning per film thickness and hence is kept thin to minimize the reduction.

#### 3.1. Microstructure and crystallinity of BZO/YBCO ML samples

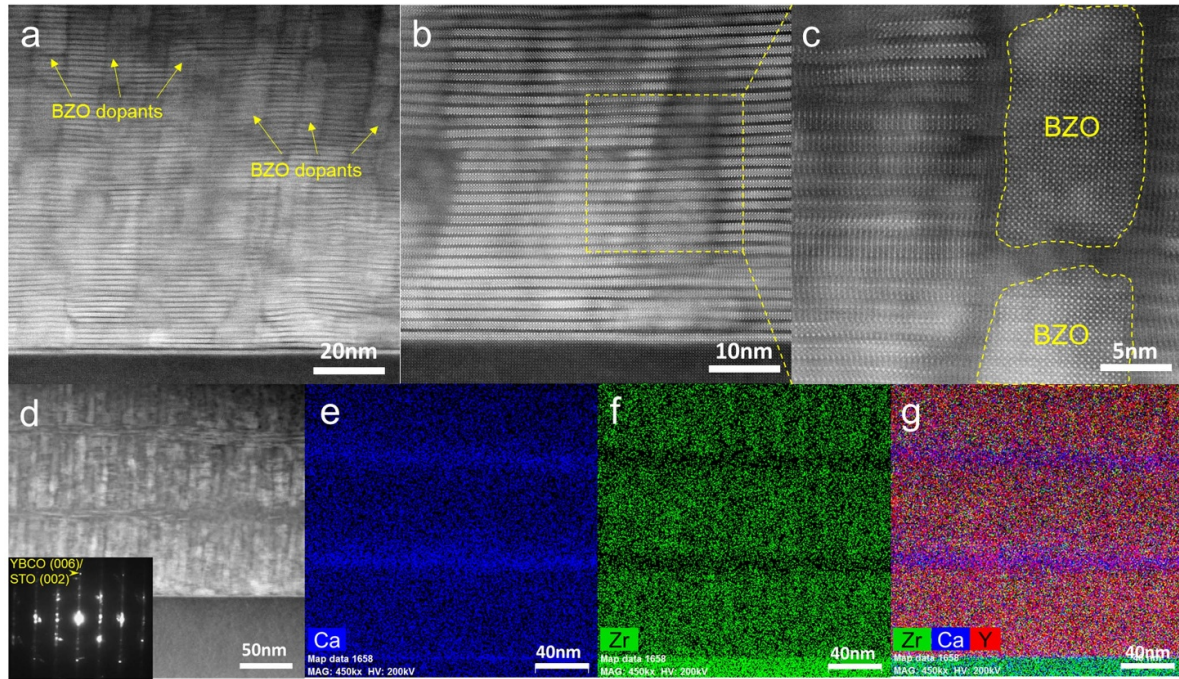
Figures 2(a)–(c) show the cross-sectional STEM images of a 6% BZO/YBCO SL film with different magnifications. BZO 1D-APCs can be clearly seen to be embedded in the YBCO film matrix as shown in figures 2(a) and (b). The HRSTEM image shown in figure 2(c) was extracted from the yellow square region highlighted in figure 2(b), illustrating vertical epitaxial growth of the cubic structured BZO nanodopants and the layered structure of YBCO. The distorted YBCO lattice is anticipated from the strain effect at the BZO 1D-APC/YBCO interface. The morphology and element distribution of a 6% BZO/YBCO ML film are illustrated in figures 2(d)–(g). BZO 1D-APCs formed through the thickness of each of the three BZO/YBCO layers. Although some of

them seem to be truncated by the CaY-123 spacers, the alignment of the BZO 1D-APCs is through the entire film thickness. This is supported by the Zr distribution shown in figure 2(f), which means the concentration of the BZO 1D-APCs in the ML sample would be comparable to that of their SL counterpart at the same BZO doping.

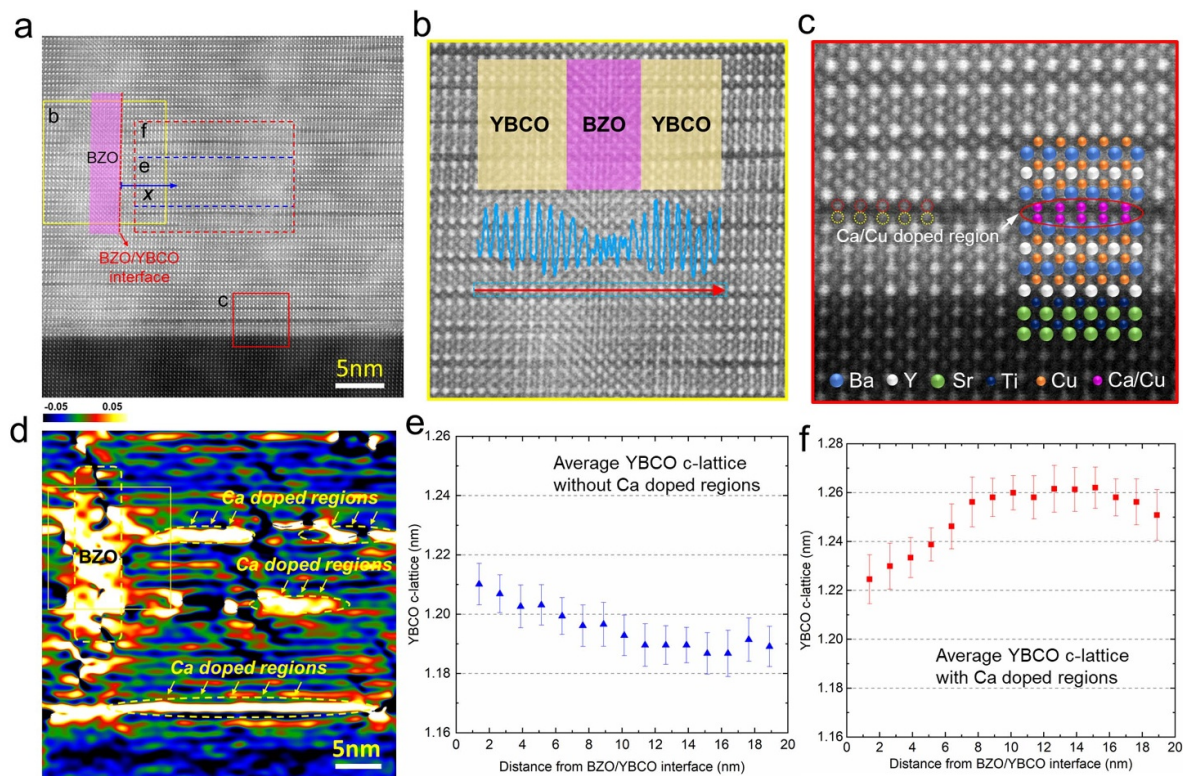
The inset in figure 2(d) illustrating a selected area electron diffraction pattern confirms the epitaxial growth of YBCO (000 $l$ ) on the (001) SrTiO<sub>3</sub> (STO) substrate. The presence of the CaY-123 spacers is confirmed both in the STEM (figure 2(d)) and the energy-dispersive x-ray spectroscopy (EDS) elemental map of Ca in figure 2(e). In addition, Ca with a much lower concentration between those spacers are observed, which suggests that only a small amount of Ca diffuses from the CaY-123 spacer to the BZO/YBCO layers. Besides those CaY-123 spacers, the Ca doping was found to be enriched at specific YBCO atomic planes in the YBa<sub>2</sub>Cu<sub>3-x</sub>Ca<sub>x</sub>O<sub>7-δ</sub> to be discussed in detail below.

To analyze the BZO nanocolumns within YBCO matrix, the HRSTEM in the high angle annular dark field mode (HRSTEM-HAADF) were taken on a 2% BZO/YBCO ML film, as shown in figure 3(a). It is noted that, to conduct high quality HRSTEM imaging analysis, a high quality lattice area without significant lattice distortion is preferred. Hence, the 2% BZO/YBCO ML rather than the 6% BZO/YBCO film was chosen for HRSTEM imaging and strain analysis. An intensity line profile was conducted to examine the phase distribution across the BZO 1D-APC/YBCO interface, as shown in figure 3(b). Clear phase separation between BZO and YBCO is observed from the contrasts in the line profile, as the contrast (image intensity  $I$ ) in STEM image intensity is proportional to the atomic number ( $Z$ ), more specifically,  $I \propto Z^{1.7}$  [42]. It is noted that the lower intensity of BZO phase is also attributed to a strain-confinement effect [43]. Figure 3(c) is the enlarged view of the red square area in figure 3(a) showing the atomic interface contact at the Ca-doped region in the BZO/YBCO layer and YBCO/STO substrate interface under the  $\langle 100 \rangle$  zone axis. The Cs-corrected HRSTEM image provides directly interpretable atomic arrangements of the cations at the interfaces, and the projected atomic arrangements of STO, YBCO with a Ca-doped Cu-O planes on YBCO lattice are superimposed on the image with different colors, as illustrated in figure 3(c). In order to identify the Ca/Cu substitution across the YBCO/STO interface and Ca-doped BZO/YBCO regions, four intensity line profiles ((a)–(d) in figure 4) have been retrieved based on the HRSTEM image in figure 3(c). The atom columns can be identified based on their different line profile intensities, where the Ca-doped regions on the YBa<sub>2</sub>Cu<sub>3-x</sub>Ca<sub>x</sub>O<sub>7-δ</sub> unit cell are represented by the wider and lower intensity ranges in the line profiles as the red dashed region indicated in figures 4(a) and (b). For comparison, two horizontal line profiles across the Cu atom columns in undoped and Ca-doped YBCO unit cells are retrieved, as shown in figures 4(c) and (d), respectively. Because of the relationship between STEM image intensity ( $I$ ) and atomic number ( $Z$ ), i.e.  $I \propto Z^{1.7}$ , the substituted Ca atomic columns demonstrate obviously lower intensity than that of Cu columns, as indicated in



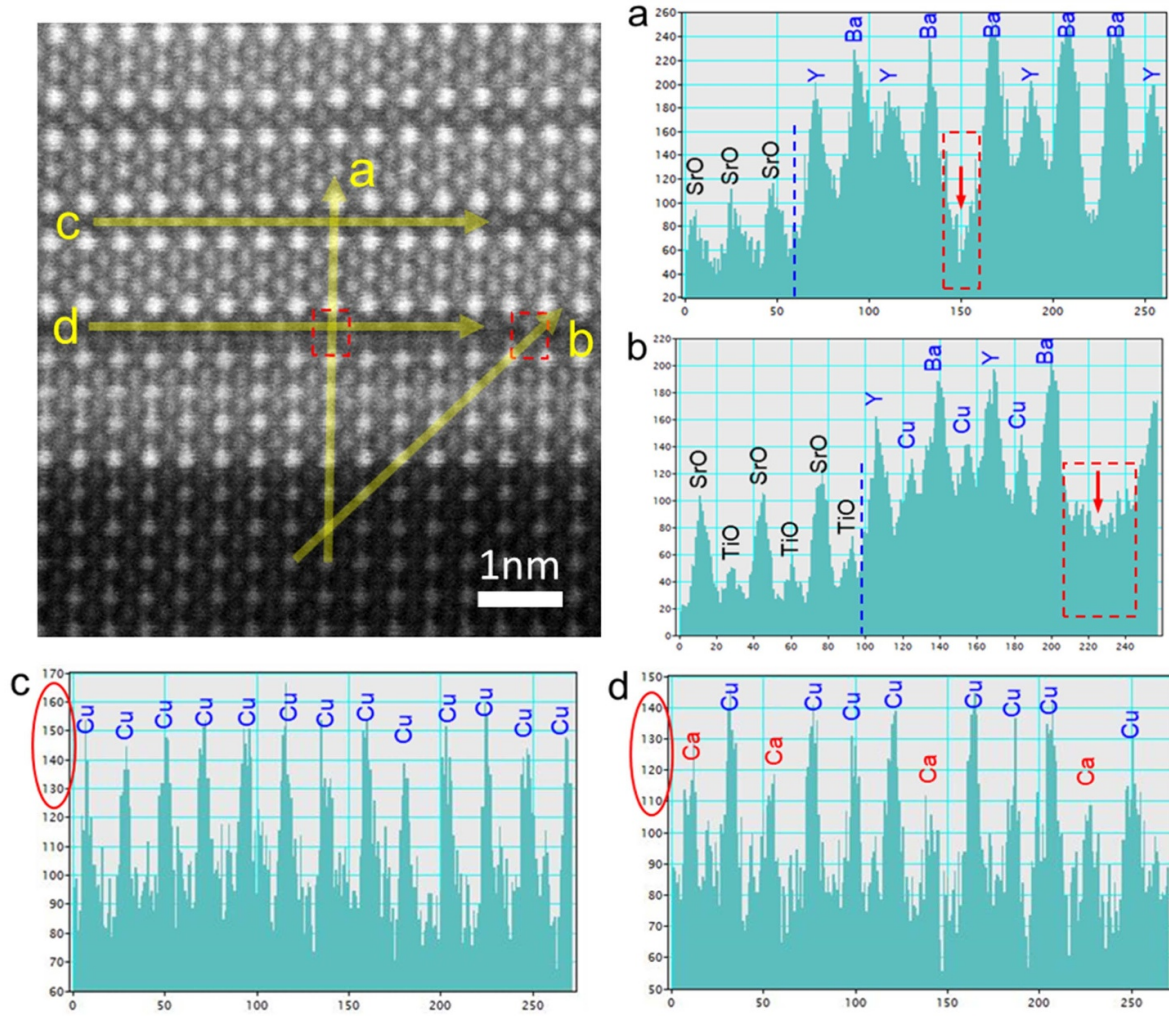


**Figure 2.** (a) Low magnification and (b), (c) high resolution cross-sectional STEM images of the 6 vol.% BZO doped single layer YBCO film. (d) Low magnification cross-sectional STEM image and (e)–(g) EDS mappings of the BZO/Ca-Y123 doped multilayer YBCO film.



**Figure 3.** (a) High resolution cross-sectional STEM image of the 2% BZO/YBCO ML film. (b) Enlarged view of the yellow square area in (a) showing the atomic lattice across the BZO/YBCO interface. The intensity line profile is conducted along the red line, where the doped BZO phase region shows weaker intensity due to the lattice strain confinement effect. (c) Enlarged view of the red square area in (a) showing the atomic interface contact at the Ca-doped region and YBCO/STO interface under the <100> zone axis. The projected atomic arrangements of YBCO, Ca doped layer and STO lattice are superimposed on the image. (d) EDS mapping of Ca, showing Ca doped regions (indicated by yellow arrows) and a 5 nm scale bar. (e) Average YBCO c-lattice without Ca doped regions. (f) Average YBCO c-lattice with Ca doped regions.





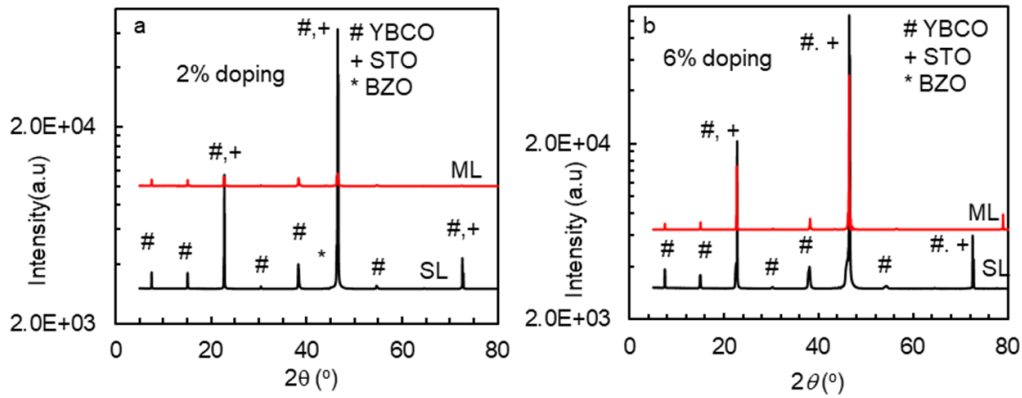
**Figure 4.** The zoom-in view of the HRSTEM image in figure 3(c) showing the atomic interface contact at the Ca-doped region in the BZO/YBCO layer and YBCO/STO interface under the  $\langle 100 \rangle$  zone axis. ((a)–(d)): The intensity line profiles across the YBCO/STO interface and Ca-doped regions within the  $\text{YBa}_2\text{Cu}_{3-x}\text{Ca}_x\text{O}_{7-\delta}$  thin film grown on STO (001) substrate. The type of the atomic columns was noted based on their different line profile intensities. The film/substrate interface and the Ca-doped regions in BZO/YBCO layer are marked respectively by the dashed line and dashed boxes to guide the view.

figure 4(d). Therefore, based on the line profiling analyses in the HRSTEM images, the Ca doping within the BZO/YBCO ML film is further confirmed.

It should be noted that the stacking faults observed in the BZO/YBCO ML samples differ from the reported ones in the  $\text{YBa}_2\text{Cu}_4\text{O}_8$  (Y124) phase [44] in both formation mechanism and microstructure. First, the stacking faults in the ML samples are induced by Ca doping, instead of Cu doping in Y124, and occur mostly near the BZO 1D-APC/YBCO interface where strong tensile strain is present due to the larger lattice constant of BZO  $\sim 7.7\%$  larger than the  $c$ -axis of undoped YBCO. On the other hand, the Ca/Cu substitution in the ML samples were observed only in the single Cu-O atomic planes, which is in contrast to continuous stacking faults throughout the entire lattice planes often extending to multiple Cu-planes (more like second phase incorporation) in the Y124 phase. Considering Y124 has a low  $T_c \sim 80$  K and could potentially degrade superconductivity if a large amount is present in the YBCO film, the smaller, segmented Ca/Cu stacking faults are

expected to have a reduced negative impact on superconductivity of the BZO/YBCO ML films. This argument is supported by the  $T_c \sim 84$  K–85 K for the ML samples being comparable to that of the BZO/YBCO SL samples, and much enhanced  $J_c$  at 65 K–77 K in ML samples as compared to their SL counterpart's.

To further explore the lattice vs. strain relationship in the BZO/YBCO layers with Ca doping, the GPA of the out-of-plane ( $\epsilon_{yy}$ ) strain mapping of the HRSTEM image in figure 3(a) was conducted and the result is shown in figure 3(d). The BZO columns and Ca-doped regions within the BZO/YBCO layers show larger  $c$ -lattice spacing with brighter contrast, while the undoped YBCO matrix and STO substrate exhibit darker contrast indicating smaller  $c$ -lattice values. Furthermore, the local strain effect can be quantified by measuring the  $c$ -axis variation of YBCO based on the HRSTEM image. Figure 3(e) shows the YBCO  $c$ -lattice constant as a function of the distance from BZO 1D-APC/YBCO interface, where the  $c$ -axis lattice constant is calculated by



**Figure 5.**  $\theta - 2\theta$  scans of SL (black) and ML50 nm/10 nm–2 Hz films (red) at BZO doping of (a) 2% and (b) 6%. The ML films were fabricated with structure or/and PLD growth conditions of:  $t_{\text{spacer}} = 10$  nm, and  $R_{\text{spacer}} = 2$  Hz. Cu- $k\alpha$  radiation of wavelength 1.54 Å was used. The symbols #, + and \* represent the YBCO (001), STO substrate (100) and major BZO (001) peaks respectively.

averaging five unit cells in the dashed blue box region shown in the STEM image in figure 3(a). The  $c$ -lattice constant of YBCO decreases gradually with increasing distance from the BZO 1D-APC/YBCO interface because of the gradually relieved interfacial strain. However, by including some Ca-doped regions on the YBCO lattice (dark contrast regions in HRSTEM image), as shown by the large dashed red box shown in figure 3(a), the average  $c$ -lattice constant of YBCO is found to increase to the maximum value then slightly decrease as away from the doped areas as going away from the BZO 1D-APC/YBCO interface. This can be explained by the compensation effect caused by the interfacial strain relaxation at the 1D-APC/YBCO interfaces and the additional  $c$ -axis enlargement induced by Ca-doping effect on the YBCO lattice. The average YBCO  $c$ -lattice constant reaches the maximum of  $\sim 1.26$  nm when these two effects are compensated as illustrated in figure 3(f).

Figures 5(a) and (b) illustrate respectively the XRD  $\theta - 2\theta$  spectra of the 2% BZO/YBCO and 6% BZO/YBCO ML films. Both ML samples have  $t_{\text{spacer}} = 10$  nm and  $R_{\text{spacer}} = 2$  Hz. For comparison, the XRD  $\theta - 2\theta$  spectra taken on the 2% BZO/YBCO and 6% BZO/YBCO SL samples (black) are also included in the figure 5. The presence of YBCO (001) peaks in all  $\theta - 2\theta$  spectra confirm that these four BZO/YBCO nanocomposite films are oriented along the  $c$ -axis along the (100) STO substrates. In addition, BZO peaks have been detected in all four spectra.

Considering the peak intensities for BZO are relatively low as compared to that of YBCO and STO, figure S1 (available online at [stacks.iop.org/SUST/35/034001/mmedia](https://stacks.iop.org/SUST/35/034001/mmedia)) depicts the original XRD spectrum taken on 6% BZO/YBCO ML50 nm/10 nm–4 Hz (see table 1) with all identified peaks including three that can only be indexed to BZO listed in table S1 (supplemental information). The  $c$ -lattice constants can be estimated from the YBCO (001) peaks. For the 2% and 6% SL films the  $c$ -lattice constants were 11.746 Å and 11.819 Å respectively, confirming the increased tensile strain with increased BZO doping most probably due to the increased strain field overlap [45, 46]. In contrast, the same  $c$ -lattice constants of 11.766 Å observed on both the 2% and 6% ML

samples suggest the benefit of the ML scheme in reducing the strain field overlap effect that increases with increasing BZO doping. It should be noted that the enlarged YBCO  $c$ -axis lattice constant occurs only locally near the BZO 1D-APC/YBCO and YBCO/STO interfaces due to formation of planer defects or stacking faults induced by Ca/Cu replacement on Cu-O planes as revealed in the HRSTEM study in figures 3 and 4. Overall, the amount of Ca diffused from the two CaY-123 spacer layers (5–15 nm in each layer) into the three BZO/YBCO layers ( $\sim 50$  nm in each layer) is small considering the total volume portion of the spacer layer is in the range of 6%–17% while a substantial portion of the Ca remained in the spacer layers as shown in figure 2(g). In fact, the ML scheme was selected in this work to achieve a controllable diffusion of a small amount of Ca to the YBCO lattice by controlling the CaY-123 spacer layer thickness and PLD conditions. Therefore, the smaller average  $c$ -lattice constants of 11.766 Å measured in XRD globally as compared to the larger ones up to 1.26 nm or 12.6 Å obtained from HRSTEM measured locally around the BZO 1D-APC/YBCO and YBCO/STO interfaces is not a surprise considering the limited amount of Ca diffused into the YBCO lattice and the occurrence of a small volume portion of short, segmented stacking faults primarily around the BZO 1D-APC/YBCO and YBCO/STO interfaces. Furthermore, the Ca/Cu replacement occurs dynamically after the formation of the BZO 1D-APCs, which means that the HRSTEM  $c$ -lattice analysis near the BZO/YBCO interface within a few nm region represents the most pronounced  $c$ -lattice elongation on the BZO/YBCO ML films. In contrast, the XRD result is an average over a larger area ( $\sim$  a few mm in dimension) of the BZO/YBCO nanocomposite films and a reduced average  $c$ -axis elongation is anticipated since the Ca/Cu replacement may not occur uniformly especially in the area not too close to the BZO/YBCO interface of less original tensile strain. A direct consequence of the local strain reduction at the BZO/YBCO interface is reduction of the microstrain. This is confirmed in the smaller full width at half maximum (FWHM) of YBCO (005) peaks on the 2% and 6% ML samples of  $0.32^\circ$  and  $0.38^\circ$  respectively as compared to  $0.36^\circ$  and  $0.59^\circ$  on their SL counterparts.

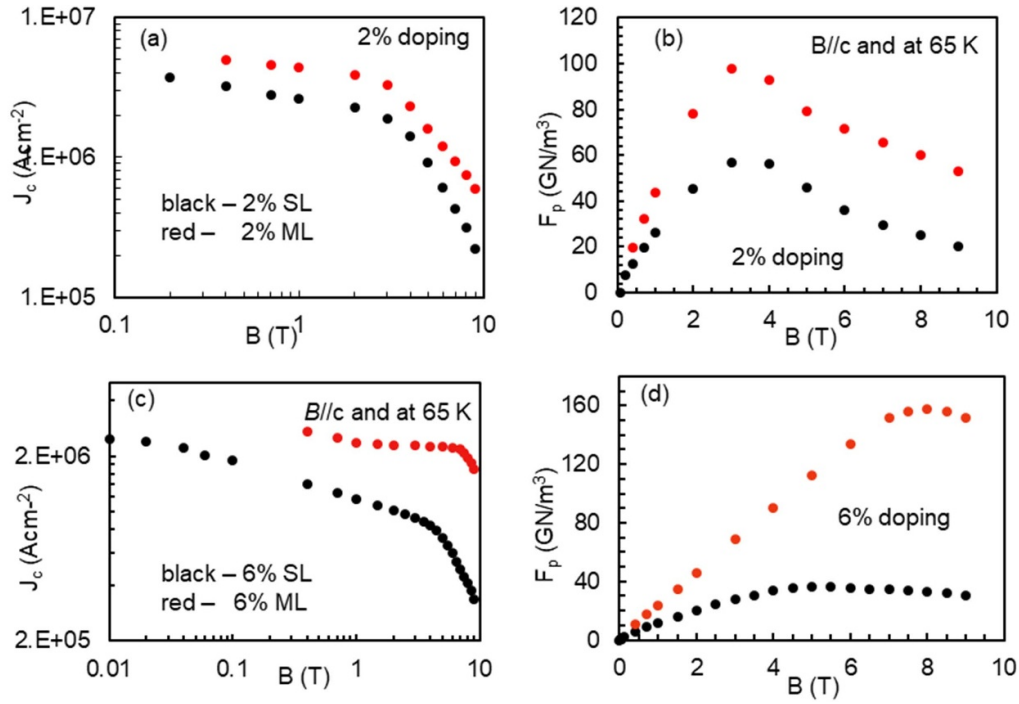


**Figure 6.**  $J_c$  vs.  $H$  and  $F_p$  vs.  $H$  curves measured along  $\theta = 0^\circ$  ( $B//c$ -axis) at 65 K on 2% BZO/YBCO (a) and (b); and 6% BZO/YBCO (c) and (d). Each panel compares an SL film (black) with an ML50 nm/10 nm–2 Hz film (red).

**Table 1.** Summary of  $T_c$ ,  $F_{p,max}$ , and  $B_{max}$  values of pristine YBCO, 2% and 6% BZO/YBCO SL and ML films at  $B//c$ -axis at 77 K and 65 K. For the ML samples, the CaY-123 thickness  $t_{spacer}$  was varied in the range of 5–15 nm, and the PLD repetition rate  $R_{spacer}$  was selected to be 1, 2 and 4 Hz, respectively. The BZO/YBCO thickness was selected to be 50 nm and 100 nm, respectively.

Sample ID	$T_{c, onset}$ (K)	$F_{p,max}$ (GN m <sup>-3</sup> )		$B_{max}$ (T)	
		77 K	65 K	77 K	65 K
Pristine YBCO	89.0	7.98	54.83	2.0	5.0
2% BZO/YBCO SL	88.5	6.14	57.09	3.0	3.0
2% BZO/YBCO ML50 nm/10 nm–2 Hz	87.5	10.67	97.73	3.0	3.0
6% BZO/YBCO SL	86.9	6.36	36.14	4.5	5.0
6% BZO/YBCO ML50 nm/10 nm–1 Hz	83.5	6.55	82.20	4.5	6.0
6% BZO/YBCO ML50 nm/10 nm–2 Hz	84.0	12.77	157.70	6.5	8.0
6% BZO/YBCO ML50 nm/10 nm–4 Hz	85.0	10.40	93.35	5.0	6.5
6% BZO/YBCO ML50 nm/15 nm–4 Hz	85.0	10.15	100.39	5.0	6.0
6% BZO/YBCO ML50 nm/5 nm–4 Hz	85.0	16.55	144.34	5.0	6.5
6% BZO/YBCO ML100 nm/10 nm–2 Hz	83.5	8.30	122.82	7.0	8.0

This result suggests that the reduction of microstrain using the ML scheme would provide more benefits to BZO/YBCO nanocomposite films at higher BZO doping when strain field overlapping becomes a more serious concern.

### 3.2. Transport $J_c$ and $F_p$ in BZO/YBCO ML samples

Figure 6 compares the critical current density  $J_c(B)$  and pinning force density  $F_p(B) = J_c \times B$  curves of the four samples shown in figure 5 measured at 65 K to avoid complication of the  $T_c$  effect at magnetic field  $B//c$ -axis. The  $T_c$  values are 88.5 K, 87.5 K, 86.9 K and 84.9 K for the 2% BZO/YBCO SL, 2% BZO/YBCO ML, 6% BZO/YBCO SL and 6% BZO/YBCO ML respectively (table 1). For both 2% and 6% BZO doping, the ML samples exhibit enhanced  $J_c(B)$

over the entire  $B$  field range of 0–9 T as compared to their SL counterparts'. In addition, the  $J_c(B)$  enhancement increases with the applied  $B$  fields. For example, an enhancement factor of 1.7 and 2.0 can be observed at 1.0 T for the 2% and 6% cases respectively, while higher enhancement factors of 2.7 and 5.0 occur at  $B = 9.0$  T (figures 6(a) and (c)). Furthermore, the  $J_c(B)$  curve for the 6% BZO/YBCO ML sample exhibits much reduced  $B$ -field susceptibility as compared with the 2% BZO/YBCO ML sample, indicating more enhanced pinning in a larger  $B$  field range as anticipated from the three times higher concentration of the BZO 1D-APCs in the former case. The improved  $J_c(B)$  leads to an improved  $F_p(B)$  in the ML samples as shown in figures 6(b) and (d).

Quantitatively, some subtle differences are clearly visible between the 2% and 6% BZO/YBCO cases. In the former



(figure 6(b)), the  $F_p(B)$  peaks for the ML and SL samples locate almost at the same locations of  $B_{\max} \sim 3.0$  T despite an enhanced  $F_{p\max}$  value by approximately 72% from  $\sim 57$  GN m $^{-3}$  for the 2% SL sample to  $\sim 98$  GN m $^{-3}$  for the 2% ML sample. In the latter (figure 6(d)), both  $B_{\max}$  and  $F_{p\max}$  are dramatically enhanced in the ML sample as compared to its SL counterpart's. In fact, the enhanced  $B_{\max} \sim 8.0$  T in the 6% BZO/YBCO ML sample is 60% higher than that of the 6% BZO/YBCO SL sample. Moreover, the enhanced  $F_{p\max} \sim 158$  GN m $^{-3}$  in the 6% ML sample is 4.4 times higher than that of the 6% SL sample. It should be noted that the  $F_{p\max}$  of  $\sim 158$  GN m $^{-3}$  at 65 K represents the best reported so far in BZO 1D-APC/YBCO nanocomposites [9, 20, 47–50]. The more dramatic enhancement of the pinning in the 6% BZO/YBCO ML sample is not surprising considering the expected benefits of improved BZO/YBCO interface and reduced strain field overlap at high concentration of the BZO 1D APCs.

### 3.3. Effects of PLD repetition rate and thickness of CaY-123 spacer and BZO/YBCO

In order to further understand the effect of Ca diffusion and the consequent Ca/Cu replacement in the ML samples, two sets of 6% BZO/YBCO ML samples made with different  $t_{\text{spacer}}$  and  $R_{\text{spacer}}$  values were investigated. Figure 7(a) compares the XRD  $\theta - 2\theta$  spectra of one set of three 6% BZO/YBCO ML samples all having two CaY-123 spacers of  $t_{\text{spacer}} = 10$  nm while the spacers were made at different  $R_{\text{spacer}}$  of 1 Hz (blue), 2 Hz (black), and 4 Hz (red) respectively. Figure 7(b) shows the XRD  $\theta - 2\theta$  spectra of the other set of three 6% BZO/YBCO ML films fabricated at the same  $R_{\text{spacer}}$  of 4 Hz with varying  $t_{\text{spacer}}$  of 5 nm (black), 10 nm (red), and 15 nm (blue). Irrespective of the  $R_{\text{spacer}}$  and  $t_{\text{spacer}}$  values, the XRD  $\theta - 2\theta$  spectra show  $c$ -axis oriented epitaxial growth of the BZO/YBCO ML films evidenced by the (001) YBCO peaks (#). As discussed above, the BZO peak intensities are relatively low and barely visible in figure 7(a) due to small amount of BZO doping in the BZO/YBCO nanocomposite samples. In order to confirm the presence of the BZO, original XRD spectra for samples in figure 7 were examined using the similar method described in figure S1 and table S1 (supplemental information). The calculated  $c$ -axis lattice constants of the films are 11.734 Å, 11.766 Å and 11.745 Å for the three 6% BZO/YBCO ML samples made with  $t_{\text{spacer}}$  of 10 nm and  $R_{\text{spacer}}$  of 1 Hz (blue), 2 Hz (black), and 4 Hz (red) respectively (figure 7(a)). In addition, the samples made with  $R_{\text{spacer}} = 4$  Hz and  $t_{\text{spacer}}$  of 5 nm (black), 10 nm (red), and 15 nm (blue) respectively have the  $c$ -axis constants of 11.762 Å, 11.745 Å and 11.734 Å respectively (figure 7(b)). Overall, the reduced  $c$ -axis lattice constants in all six 6% BZO/YBCO ML samples as compared to the 11.819 Å of the reference 6% BZO/YBCO SL sample confirm the reduced strain field by the dynamic Ca/Cu replacement preferentially at the BZO/YBCO interface of the highest strain field. This argument is supported by the smaller FWHMs of the YBCO (005) peaks for the ML samples as compared to their SL counterpart's. Specifically, the FWHM values are 0.26°, 0.38° and 0.38° for the 6% BZO/YBCO ML

samples made with  $t_{\text{spacer}}$  of 10 nm and  $R_{\text{spacer}}$  of 1 Hz (blue), 2 Hz (black), and 4 Hz (red) respectively in figure 7(a). Similarly, the FWHM values are 0.34°, 0.38° and 0.34° for the 6% BZO/YBCO ML samples made with  $R_{\text{spacer}} = 4$  Hz and  $t_{\text{spacer}}$  of 5 nm (black), 10 nm (red), and 15 nm (blue) respectively (figure 7(b)). This is in contrast to the FWHM  $\sim 0.59^\circ$  of the reference 6% BZO/YBCO SL film. This result indicates the reproducibility of the ML approach to induce a dynamic Ca/Cu replacement and elongated  $c$ -axis lattice constant at and near the BZO 1D-APC/YBCO interface for improved interface and overall crystallinity of the BZO/YBCO nanocomposite films especially at high BZO doping.

While the XRD data suggests that the six 6% BZO/YBCO MLs samples have comparable crystalline structures and microstrain in average, differences in pinning properties have been observed with respect to the sample structures or/and PLD conditions. Figure 8 compares the  $J_c(B)$  and  $F_p(B)$  curves of the three 6% ML samples shown in the figure 8(a) with their 6% SL reference sample at 77 K and 65 K respectively. The pinning improvement in the ML samples (colored) can be clearly seen as compared to the reference SL case (black) [19, 51, 52], especially at high  $B$  fields and the lower temperature (to avoid the  $T_c$  effect). At the fixed  $t_{\text{spacer}} = 10$  nm and varying  $R_{\text{spacer}}$  from 1 Hz (purple), to 2 Hz (red), and to 4 Hz (blue), the effective diffusion time of the Ca decreases monotonically. While this does not generate a significant effect on the XRD result that reflects the macroscopic average over the ML samples, the pinning efficiency of the BZO 1D-APCs is sensitively affected by the subtle difference of the Ca diffusion at a microscopic scale as shown in figure 8. At 77 K, the three ML samples have their self-field  $J_c$  values in the range of 1.3–2.2 MA cm $^{-2}$  that are comparable but slightly higher than the 0.93 MA cm $^{-2}$  recorded for the SL reference sample. The slightly lower self-field  $J_c$  in the SL sample is actually common and consistent with the reported results in literature due to the high strain at 6 vol.% BZO doping that typically reduces the  $T_c$  of the BZO 1D-APC/YBCO nanocomposite monotonically with the increasing BZO content [21, 53]. For this specific SL sample, the  $T_c$  of 86.9 K is higher than the  $T_c$  values of its ML counterparts of 83.5 K (1 Hz), 84.0 K (2 Hz) and 85.0 K (4 Hz) as shown in table 1. The increasing  $T_c$  values with increasing  $R_{\text{spacer}}$  may be attributed to the decreasing Ca diffusion in the YBCO lattice [22, 23]. Therefore, the increasing Ca diffusion into the YBCO lattice, either through increasing the amount of the Ca in the two CaY-123 spacers or increasing the Ca diffusion time by reducing the PLD repetition rate, will lead to a compromise of the two opposite effects: reduction of the  $T_c$  value and improvement of  $J_c$  and  $F_p$  through improving the microstructure of the BZO/YBCO interface. The former would have a negative impact on the  $J_c(B)$  and  $F_p(B)$  at temperatures close to the  $T_c$ , which explains the lowest  $T_c$  of 83.5 K at for the ML sample made with  $R_{\text{spacer}} = 1$  Hz and negligible improvement of the  $J_c(B)$  and  $F_p(B)$  of this sample as compared to the SL counterpart's at 77 K. At 65 K at which the  $T_c$  effect is no longer significant, the effect of the improvement of BZO/YBCO interface becomes dominant and all three ML samples show significantly enhanced  $J_c(B)$  and  $F_p(B)$  than their SL counterpart's in

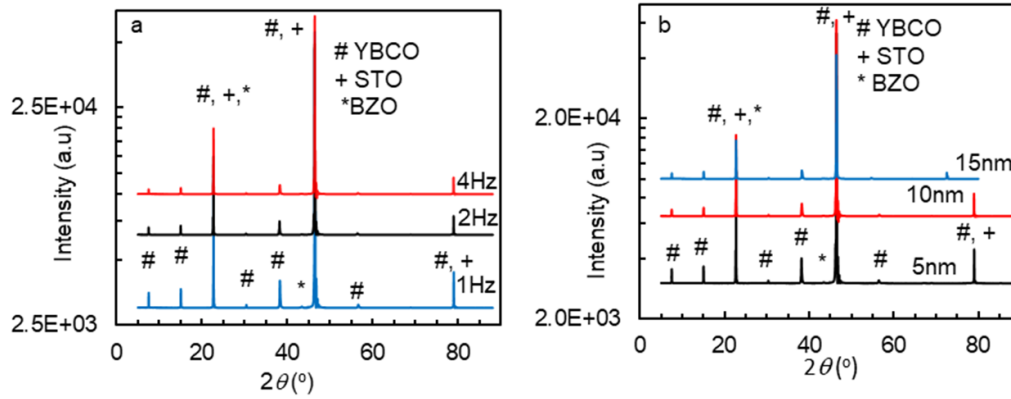


**Figure 7.**  $\theta - 2\theta$  XRD scans of 6% ML samples with different structure or/and PLD growth conditions of: (a)  $t_{\text{spacer}} = 10$  nm, and  $R_{\text{spacer}} = 1$  Hz (blue), 2 Hz (black) and 4 Hz (red); and (b)  $R_{\text{spacer}} = 4$  Hz, and  $t_{\text{spacer}} = 5$  nm (black), 10 nm (red) and 15 nm (blue), respectively. Cu- $\alpha$  radiation of wavelength 1.54 Å was used. The symbols #, + and \* represent the YBCO (001), STO substrate (100) and major BZO (001) peaks respectively.

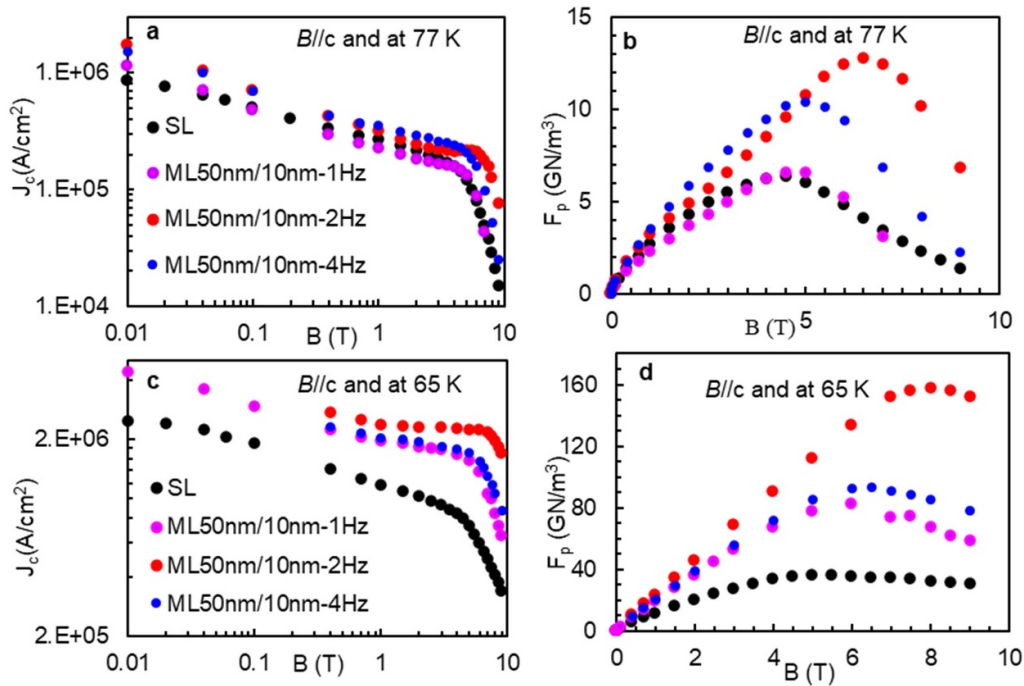


**Figure 8.**  $J_c$  vs.  $B$  and  $F_p$  vs  $B$  curves measured on a 6 vol.% BZO/YBCO named as SL (black) and three multilayer samples: ML50 nm/10 nm–1 Hz (purple), ML50 nm/10 nm–2 Hz (red) and ML50 nm/10 nm–4 Hz (blue) at  $\theta = 0^\circ$  ( $B//c$ -axis) (a) and (b) at 77 K, and (c) and (d) at 65 K respectively. The same color codes are followed in all figures.

the entire range of the field up to 9.0 T (figures 8(c) and (d)) despite their lower  $T_c$ 's. This confirms the enhanced pinning efficiency of BZO 1D-APCs in the ML samples. Quantitatively, the best pinning improvement was observed on the 6% ML (10 nm–2 Hz) sample at both 77 K and 65 K (red) among the three 6% ML samples in figures 8(a) and (c), indicating the optimal Ca-diffusion is a compromise of the two opposite effects of improving  $J_c$  and  $F_p$  (positive) through improving the BZO 1D-APC/YBCO interface and reduction of the sample  $T_c$  (negative) as anticipated in Ca-doped YBCO. The enhanced pinning is further illustrated in the right shift of the  $B_{\text{max}}$  values in the 6% ML samples as compared to their SL

reference's. Specifically, the  $B_{\text{max}}$  values are 4.5 T and 5.0 T–6.5 T at 77 K respectively for the 6% SL sample and ML samples. At 65 K, they are 5.0 T and 6.0–8.0 T respectively (table 1), indicating a considerable portion of the BZO 1D-APCs are activated in the ML samples to enable their contribution to pinning at high  $B$  fields.

Figure 9 exhibits the  $J_c(B)$  and  $F_p(B)$  curves of the three 6% ML samples with fixed  $R_{\text{spacer}} = 4$  Hz and variable  $t_{\text{spacer}} = 5$  nm (green), 10 nm (red) and 15 nm (blue) at 77 K and 65 K (figure 7(b)). Interestingly, all three ML samples have the same  $T_c \sim 85.0$  K, indicating the Ca diffusion and the Ca/Cu replacement on the YBCO lattice may only be affected by the

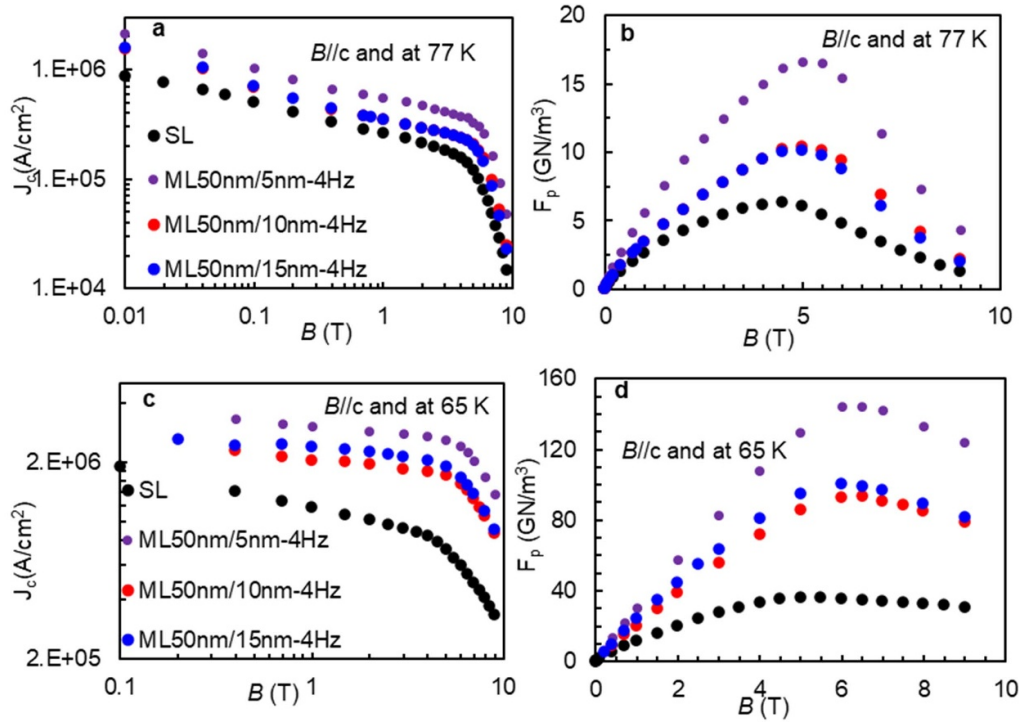


**Figure 9.**  $J_c$  vs.  $B$  and  $F_p$  vs.  $B$  curves measured on 6 vol.% BZO/YBCO named as SL (black) and multilayer samples: ML50 nm/5 nm–4 Hz (green), ML50 nm/10 nm–4 Hz (red) and ML50 nm/15 nm–4 Hz (blue) fabricated at same RR of 4 Hz at  $\theta = 0^\circ$  ( $B$ // $c$ -axis) (a) and (b) at 77 K and (c) and (d) at 65 K respectively. Color codes follow the same for all figures.

CaY-123 spacer thickness moderately. In fact, since the CaY-123 spacer truncate the BZO 1D-APCs into segments, smaller  $t_{\text{spacer}}$  is more favorable to a higher specific pinning force (pinning force per film thickness). Overall, all three ML samples have overall higher  $J_c(B)$  and  $F_p(B)$  in the entire magnetic field range up to 9.0 T than their SL counterpart at both 77 K and 65 K. Particularly at 65 K, the enhancement is more pronounced at higher fields. For example, the  $J_c(B)$  (and  $F_p(B)$ ) enhancement factor at 1.0 T is up to 2.0, while they increase to 5.0 at 9.0 T. An interesting observation is that the 6% ML (5 nm) sample has significantly higher  $J_c(B)$  and  $F_p(B)$  than the other two ML samples with thicker CaY-123 layers, suggesting that the Ca provided in the two 5 nm thick CaY-123 spacers is adequate to induce the required  $c$ -axis elongation primarily at the BZO 1D-APC/YBCO interface on the three 50 nm thick BZO/YBCO layers. Thicker CaY-123 spacers may reduce the specific pinning force (per unit length of 1D APCs) since the spacer layer would truncate the 1D APCs into segments [24, 54].

It should be noted that the ML scheme may be applied to BZO 1D-APC/YBCO nanocomposite films with larger thickness for an enhanced critical current  $I_c$  as required for practical applications. This may be realized by: (a) increasing the number of the CaY-123 spacers while maintaining the BZO/YBCO thickness unchanged; (b) increasing the thickness of the BZO/YBCO layers at the fixed number and thickness of CaY-123 spacers; (c) a combination of (a) and (b). In an exploration of the scheme (b), 6% ML samples with the BZO/YBCO layer thickness increased to 100 nm while the film structure would be otherwise unchanged have been explored and the result is

illustrated in table 1 (last row). In comparison with its thinner counterpart of the same five-layer structure and PLD condition (6% BZO/YBCO ML50 nm/10 nm–2 Hz), a comparable but slightly lower  $T_c$  of 83.5 K (by 0.5 K) was obtained. Similarly, a slightly reduced pinning properties suggest that the ML scheme may be applied to thicker BZO/YBCO nanocomposite films while further optimization of the ML growth condition is necessary.

### 3.4. Effect of a coherent BZO/YBCO interface on pinning efficiency of BZO 1D-APCs

Figure 10 illustrates the ratios of  $F_{p,\text{max}}(\text{ML})/F_{p,\text{max}}(\text{SL})$  (black) and  $B_{\text{max}}(\text{ML})/B_{\text{max}}(\text{SL})$  (red) as a function of (a)  $R_{\text{spacer}}$  and (b)  $t_{\text{spacer}}$  at 77 K (solid) and 65 K (open). Overall, the values of the both ratios are exceeding ‘1’, suggesting the enhanced pinning efficiency of BZO 1D-APCs in the ML samples. While the  $F_{p,\text{max}}$  enhancement peaks at  $R_{\text{spacer}} = 2$  Hz (figure 10(a)), the  $F_{p,\text{max}}$  enhancement decreases monotonically with increasing  $t_{\text{spacer}}$  (figure 10(b)). The maximum enhancement factors are 4.4 (at  $R_{\text{spacer}} = 2$  Hz and  $t_{\text{spacer}} = 10$  nm) and 4.0 (at  $t_{\text{spacer}} = 5$  nm,  $R_{\text{spacer}} = 4$  Hz), respectively. Although there is no significant  $B_{\text{max}}$  enhancement with varying  $t_{\text{spacer}}$  in the range of 5–15 nm (figure 10(b), figure 10(a)) suggests that the peak  $B_{\text{max}}$  enhancement is at  $R_{\text{spacer}} = 2$  Hz as a compromise of the reduced  $T_c$  and improved pinning in the BZO/YBCO ML samples.

The improved pinning of the BZO 1D-APCs in the ML samples can extend to the other orientations of the  $B$  field away from  $B$ // $c$ -axis ( $\theta = 0^\circ$ ) as illustrated in figure 11 that



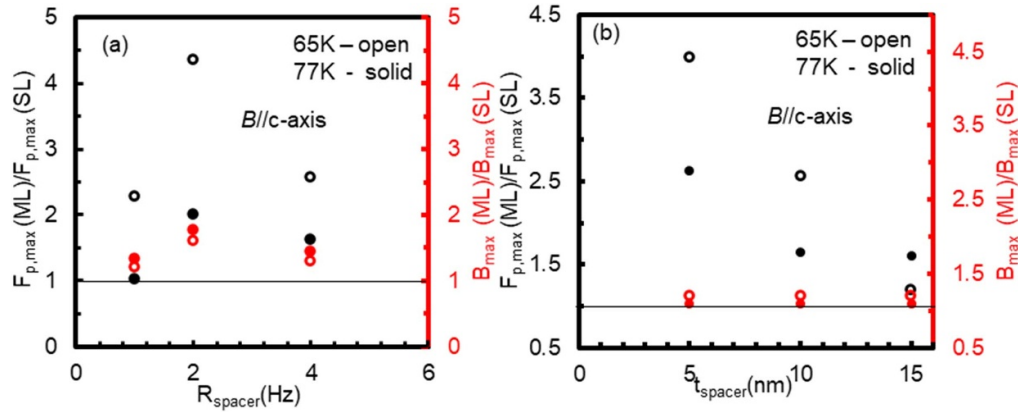


**Figure 10.** (a) Laser repetition rate (Hz) dependence of ratio of the  $F_{p,max}$  (ML)/ $F_{p,max}$  (SL) (black) on left Y-axis and  $B_{max}$  (red) on right Y-axis measured at 77 K (solid) and at 65 K (open), on B//c-axis of multilayers film (b) CaY-123 spacer layer thickness dependence of ratio of the  $F_{p,max}$  (ML)/ $F_{p,max}$  (SL) (black) on left Y-axis and  $B_{max}$  (red) on right Y-axis measured at 77 K (solid) and at 65 K (open), on B//c-axis of multilayers film.

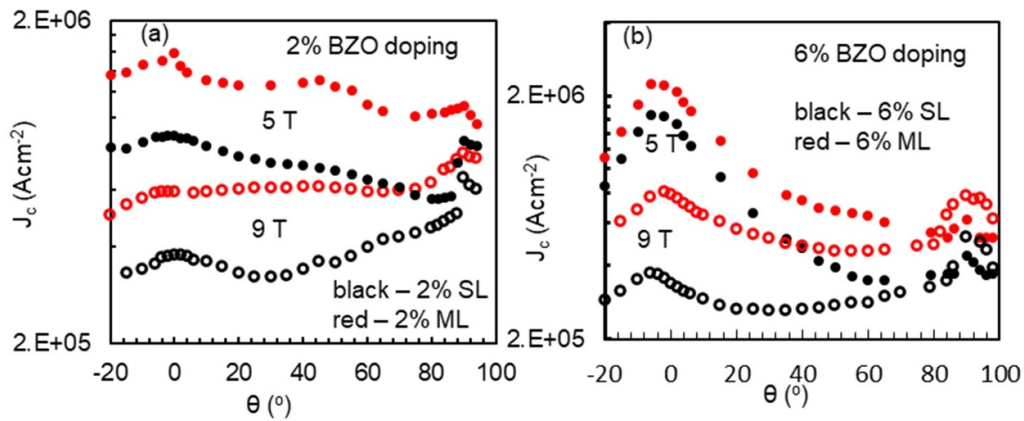


**Figure 11.**  $J_c(\theta)$  data measured at 65 K on (a) 2% BZO/YBCO and (b) 6% BZO/YBCO SL(black) and ML(red) films. The ML samples were made at  $t_{spacer} = 10$  nm and  $R_{spacer} = 2$  Hz.

compares the  $J_c(\theta)$  for the four samples shown in figure 6. Specifically, the  $J_c(\theta)$  curves of the 2% (figure 11(a)) and 6% (figure 11(b)) BZO/YBCO ML (red) and SL (black) samples are compared at 65 K at  $B$  fields of 5.0 T (s) and 9.0 T (solid), respectively. Overall, both ML samples have significantly higher  $J_c$  than its SL counterparts' in almost the entire  $\theta$  range. For example, the  $J_c(\theta)$  of 2% ML sample is about 1.9 times of that for the SL counterpart in the  $\theta$  range of  $0^\circ$ – $86^\circ$  at 5.0 T. At 9.0 T, the ML over SL  $J_c(\theta)$  enhancement factor is in the range of 1.4–1.6 within the  $\theta$  range of  $0^\circ$ – $88^\circ$ . At the higher BZO doping of 6 vol.%, the ML sample again has higher  $J_c(\theta)$  than its SL counterpart over the  $\theta$  range of  $0^\circ$ – $84^\circ$  with the highest enhancement factors of 2.8 at 5.0 T and 4.5 at 9.0 T respectively. It should be noted that a similar broad angular range  $J_c(\theta)$  enhancement has been observed in the BHO 1D-APC/YBCO nanocomposite films [55, 56], which is ascribed to high pinning efficiency due to the coherent BHO 1D-APC/YBCO interface [47, 57].

The  $N$  values that are proportional to the pinning potential barrier energy associated to the BZO 1D-APCs, were extracted through fitting the measured current–voltage ( $I$ – $V$ ) curves

using the formula of  $V \propto I^N$  [41], can provide a quantitative evaluation of the pinning potential energy of the BZO 1D-APCs in the SL and ML samples [41]. For a direct comparison, figure 12 shows the  $N$  values of the 2% (black) and 6% (red) BZO/YBCO ML samples, both were made at  $t_{spacer} = 10$  nm and  $R_{spacer} = 2$  Hz, normalized to their SL counterpart's at 65 K at which the  $T_c$  effect is insignificant. In the entire  $B$  field range, the normalized  $N$  values are larger than 1 for both 2% and 6% ML samples, indicating improved pinning potential energy in the ML samples via Ca diffusion. enhanced pinning in BZO/YBCO ML samples illustrates the direct effect of the BZO/YBCO interface on the pinning efficiency of BZO 1D-APCs.

### 3.5. Mechanism of Ca diffusion in BZO/YBCO ML samples

Considering the lattice constant of cubic structured BZO ( $3a = 1.26$  nm) is larger than that of the  $c$ -axis of YBCO ( $c = 1.17$  nm) with a  $\sim 7.7\%$  lattice mismatch, a partial Ca/Cu replacement on Cu–O planes which leads to formation of stacking faults as illustrated schematically in figure 1(b)

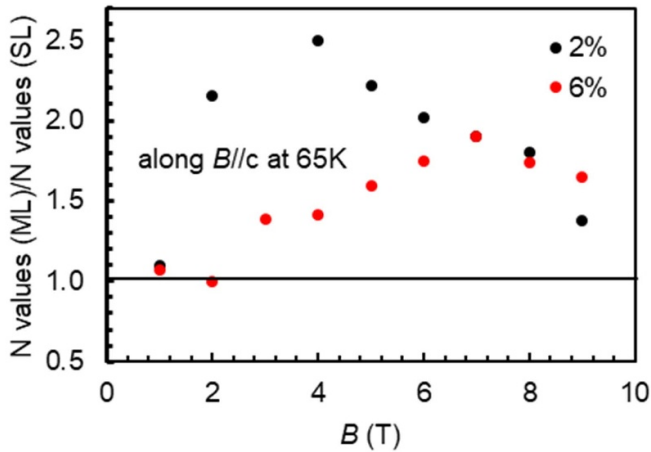


**Figure 12.** Magnetic field dependence of the  $N$  values of the 2% (black) and 6% (red) BZO/YBCO ML samples to the  $N$  values normalized to that of their SL counterparts at  $B//c$  and 65 K. The ML samples were made at  $t_{\text{spacer}} = 10$  nm and  $R_{\text{spacer}} = 2$  Hz.

**Table 2.** Valence and ionic radius for Ca, Cu, Ba, and Y ions.

Element	Valence	Ionic radius (Å)
Ca	+2	0.99
Cu	+2	0.76, 0.87
Ba	+2	1.34
Y	+3	0.89

would be energetically preferred, as compared to other possible cation exchanges of Ca/Y and Ca/Ba, on the YBCO lattice due to the presence of a tensile strain in the  $c$ -axis after the BZO 1D-APCs form in the BZO/YBCO ML films. This means the preferred Ca cation replacement is strain-dependent, as predicted in a theoretical simulation on the Ca-doping effect of YBCO bulks using Density Function Theory [58]. One may also consider the Hume-Rothery Rules when pondering the substitution of Ca for Cu in the YBCO crystal structure. While these rules are traditionally considered for determining unlimited solubility of metal alloys, they can also be applied to compounds and ceramics. The Hume-Rothery Rules list four conditions to consider: size of the atoms or ions should be  $\leq 15\%$  to minimize strain in the crystal lattice resulting from lattice mismatch, the atoms or ions should have the same crystal structure, the ions should have the same valence, and the ions should have similar electron negativities. Table 2 shows the valence and ionic radius for Ca, Cu, Ba, and Y ions [59–61]. Without any strain,  $\text{Ca} + 2/\text{Y} + 3$  substitution would be the most favored energetically considering the smallest difference of  $\sim 11\%$  in the ionic radii of  $\text{Ca} + 2$  and  $\text{Y} + 3$ , which is consistent to the reported Ca/Y substitution in YBCO for the overdoping effect due to the valence difference in  $\text{Ca} + 2$  and  $\text{Y} + 3$  [22].  $\text{Ca} + 2/\text{Cu} + 2$  substitution seems to be the next most favored energetically and the charge, mass, and crystallographic sites are maintained in this substitution.  $\text{Ca} + 2/\text{Cu} + 2$  substitution seems to be the next most favored energetically and the charge,

mass, and crystallographic sites are maintained in this substitution. We hypothesize that  $\text{Ca} + 2/\text{Cu} + 2$  substitution may become more energetically favorable than  $\text{Ca} + 2/\text{Y} + 3$  on the tensile strained BZO/YBCO considering  $\text{Ca} + 2$  could be up to 30% larger than  $\text{Cu} + 2$  and could induce lattice elongation and reduce elastic strain energy. Therefore, the Ca/Cu replacement in  $\text{YBa}_2\text{Cu}_{3-x}\text{Ca}_x\text{O}_{7-\delta}$  would result in an enlargement of the  $c$ -axis lattice constant, and the maximum Ca diffusion is expected to occur at the BZO 1D APCs/YBCO interface (the highest strain expected) before defect formation.

It should be noted that multilayers containing YBCO and Ca-doped YBCO constituent layers have been reported on bicrystal substrates to reduce the obstruction of the grain boundary (GB) on the so-called inter-grain  $J_c$  that depends exponentially on the GB angle and hence is significantly reduced from the intra-grain  $J_c$  of YBCO [22]. The local Ca diffusion into the GB is to overdope GB (by replacing  $\text{Y} + 3$  with  $\text{Ca} + 2$ ) beyond the optimal YBCO in order to reduce the build-in potential and hence the GB's tunneling barrier's height and width to reduce GB's obstruction on the inter-grain  $J_c$ . Nevertheless, the enhanced inter-grain  $J_c$  in these multilayer bicrystal YBCO films is still much below the intra-grain  $J_c$  for YBCO. In addition, the  $J_c$  investigated is primarily self-field  $J_c$ , which was shown to reach  $4.3 \times 10^5$  A cm $^{-2}$  at 77 K in multilayer YBCO films on bicrystal substrates of  $24^\circ$  GB angle. However, the microscopic mechanism in role of Ca in BZO/YBCO ML samples reported in this manuscript differs fundamentally. Specifically, the effect of Ca is to generate planar defects on YBCO for an enlarged  $c$ -axis lattice constant near the BZO/YBCO interface via formation of stacking faults through strain facilitated Ca/Cu replacement on YBCO lattice, and hence to dynamically reduce the lattice mismatch at the interface. Consequently, a reduced BZO/YBCO interface strain is obtained, which prevents formation of the defects at the interface. This allows us to achieve highly coherent BZO/YBCO interface, for the first time to our knowledge, and to probe the correlation between the BZO 1D-APC/YBCO interface and pinning efficiency of the BZO 1D-APC. The significantly enhanced pinning efficiency of the BZO 1D-APCs in the BZO/YBCO ML samples, as compared to case of their SL counterpart, illustrate that a coherent BZO/YBCO interface of negligible degradation of superconductivity is the key to high pinning efficiency of 1D-APCs.

It should also be pointed out that the ML samples reported in this work also differ from the ML samples with non-Ca containing YBCO spacers whether or not doped with APCs [62, 63]. In all these cases, segmented nanorods of BZO, BHO and BSO have been observed, resulting in reduced pinning anisotropy (reduced  $J_c$  at  $B//c$ -axis and enhanced  $J_c$  at other angles) with respect to the applied magnetic field due to the pinning by the segmented nanorod ends, or/and by other types of APCs such as nanoparticles. In the BHO-YBCO ML case, for example, the authors reported  $F_{p\text{max}}$  of  $\sim 52$  GN m $^{-3}$  and  $64$  GN m $^{-3}$  (at  $B//c$ -axis) in the ML and SL film respectively. In contrast, we observed an opposite trend of higher  $F_p$  in the ML samples than in their SL counterparts. For example, the  $F_{p\text{max}} \sim 158$  GN m $^{-3}$  in the 6% BZO/YBCO ML sample

represents about 440% enhancement over  $F_{p,max} \sim 36 \text{ GN m}^{-3}$  for the 6% BZO/YBCO SL counterpart.

The ML approach reported in this manuscript has achieved both coherent BZO 1D-APC/YBCO interface for high APC pinning efficiency and low strain field overlap on the APC/YBCO lattice for negligible (or low) degradation of the superconductivity on YBCO lattice through dynamic elongation of the YBCO  $c$ -axis via formation of stacking faults using Ca/Cu substitution on YBCO lattice locally around the BZO 1D-APC/YBCO interface. The resulted reduction of the BZO/YBCO lattice mismatch to as small as  $\sim 1.4\%$  and hence reduced BZO/YBCO interface strain results in not only a coherent BZO/YBCO interface but also a moderate strain field overlap, as reflected in the  $T_c$  values of 6 vol.% BZO/YBCO ML samples in the range of 84 K–85 K as shown in table 1, and improved  $J_c$  and  $F_p$  in the ML samples. For example, the 2% ML BZO/YBCO has  $F_{p,max}$  up to  $97.7 \text{ GN m}^{-3}$  at 65 K is 27% higher than the  $F_{p,max} \sim 76.9 \text{ GN m}^{-3}$  for 2% SL BHO/YBCO [34]. The  $F_{p,max} \sim 158 \text{ GN m}^{-3}$  at 65 K observed on 6% ML BZO/YBCO represents the best so far achieved on BZO/YBCO nanocomposites, which represents  $\sim 440\%$  improvement over  $F_{p,max} \sim 36.1 \text{ GN m}^{-3}$  on its 6% SL BZO/YBCO counterpart, not to mention the low  $F_p$  in the 6% SL BHO/YBCO by orders of magnitude. This result confirms the importance of both APC/YBCO interface and strain-field overlap (and hence superconductivity) in design APCs with high pinning efficiency.

#### 4. Conclusion

In this work, a dynamic lattice enlargement approach on YBCO matrix has been developed to enlarge its  $c$ -axis lattice constant to  $\sim 1.26 \text{ nm}$  from  $1.17 \text{ nm}$ , primarily at the BZO 1D-APC/YBCO interface during the formation of the BZO 1D-APCs in the 2%–6% BZO/YBCO nanocomposite films. The elongated YBCO  $c$ -axis lattice constant was achieved through formation of short, segmented stacking faults at the single Cu-O planes of YBCO with a partial Ca/Cu replacement. The Ca source is provided from the two CaY-123 spacers of 5–15 nm in thickness inserted into the 2%–6% BZO/YBCO nanocomposite films of 150 nm in total thickness to form the ML structures. The Ca diffusion into the tensile strained YBCO and follow-up Ca/Cu partial substitution on the single Cu-O planes of YBCO lattice is driven by the tensile strain originated from the BZO 1D-APC/YBCO interface due to the large lattice mismatch of  $\sim 7.7\%$  and is energetic favored through the resulted elongation of the  $c$ -axis of YBCO to reduce the interface strain as the BZO/YBCO lattice mismatch is decreased to  $\sim 1.4\%$ . This leads to a coherent BZO 1D-APC/YBCO interface as confirmed in microstructure analysis using HRTEM. A significantly improved pinning efficiency of the BZO 1D-APCs has been obtained in the ML samples. For example, the  $J_c(B)$  of the 6% BZO/YBCO ML samples at both temperatures of 77 K and 65 K are five times of that on the SL counterpart at 9.0 T. In addition, the  $F_{p,max} \sim 158 \text{ GN m}^{-3}$  at  $B_{max} \sim 8.0 \text{ T}$  and 65 K of the 6% BZO/YBCO ML samples represents 4.4 times of the  $F_{p,max} \sim 36 \text{ GN m}^{-3}$  (only at  $B_{max} \sim 5.0 \text{ T}$ ) of the SL

film. The enhanced pinning efficiency of the BZO 1D-APCs is illustrated also by the enhanced  $N$  values in the ML samples peaked near the  $B_{max}$ 's by up to a factor of 1.9–2.5. This result indicates the critical importance in achieving a coherent 1D-APC/YBCO interface in the APCs/YBCO nanocomposites for an optimal pinning.

#### Data availability statement

The data that support the findings of this study are available upon reasonable request from the authors.

#### Acknowledgments

This research was supported in part by US National Science Foundation contracts Nos. NSF-DMR-1508494, NSF-ECCS-1809293, NSF-DMR-1909292, the AFRL Aerospace Systems Directorate, and the Air Force Office of Scientific Research (AFOSR) LRIR #18RQOR100. D Z and H W acknowledge the support from the U.S. National Science Foundation for the high-resolution STEM effort at Purdue University (DMR-1565822 and DMR-2016453).

#### ORCID iDs

Judy Z Wu  <https://orcid.org/0000-0001-7040-4420>  
Victor Ogunjimi  <https://orcid.org/0000-0001-5111-7004>  
Bibek Gautam  <https://orcid.org/0000-0002-3406-8965>  
Haiyan Wang  <https://orcid.org/0000-0002-7397-1209>

#### References

- [1] Larbalestier D, Gurevich A, Feldmann D M and Polyanskii A 2001 High-T-c superconducting materials for electric power applications *Nature* **414** 368–77
- [2] Goyal A 2005 *Second-Generation HTS Conductors* (Berlin: Springer)
- [3] Foltyn S R, Civale L, Macmanus-Driscoll J L, Jia Q X, Maiorov B, Wang H and Maley M 2007 Materials science challenges for high-temperature superconducting wire *Nat. Mater.* **6** 631–42
- [4] Macmanus-Driscoll J L, Foltyn S R, Jia Q X, Wang H, Serquis A, Civale L, Maiorov B, Hawley M E, Maley M P and Peterson D E 2004 Strongly enhanced current densities in superconducting coated conductors of  $\text{YBa}_2\text{Cu}_3\text{O}_{7-x} + \text{BaZrO}_3$  *Nat. Mater.* **3** 439–43
- [5] Matsumoto K, Horide T, Osamura K, Mukaida M, Yoshida Y, Ichinose A and Horii S 2004 Enhancement of critical current density of YBCO films by introduction of artificial pinning centers due to the distributed nano-scaled  $\text{Y}_2\text{O}_3$  islands on substrates *Physica C* **412** 1267–71
- [6] Kang S et al 2006 High-performance high-T-c superconducting wires *Science* **311** 1911–4
- [7] Horide T, Taguchi K, Matsumoto K, Matsukida N, Ishimaru M, Mele P and Kita R 2016 Influence of matching field on critical current density and irreversibility temperature in  $\text{YBa}_2\text{Cu}_3\text{O}_7$  films with  $\text{BaMO}_3$  ( $M = \text{Zr, Sn, Hf}$ ) nanorods *Appl. Phys. Lett.* **108** 082601
- [8] Chen S, Sebastian M A, Gautam B, Wilt J, Haugan T, Xing Z and Wu J 2017 Enhancement of isotropic pinning force in



- YBCO films with BaZrO<sub>3</sub> nanorods and Y<sub>2</sub>O<sub>3</sub> nanoparticles *IEEE Trans. Appl. Supercond.* **27** 4–8
- [9] Wee S H, Zuev Y L, Cantoni C and Goyal A 2013 Engineering nanocolumnar defect configurations for optimized vortex pinning in high temperature superconducting nanocomposite wires *Sci. Rep.* **3** 2310
  - [10] Baca F J, Haugan T J, Barnes P N, Holesinger T G, Maiorov B, Lu R, Wang X, Reichart J N and Wu J Z 2013 Interactive growth effects of rare-earth nanoparticles on nanorod formation in YBa<sub>2</sub>Cu<sub>3</sub>O<sub>x</sub> thin films *Adv. Funct. Mater.* **23** 4826–31
  - [11] Mele P, Matsumoto K, Ichinose A, Mukaida M, Yoshida Y, Horii S and Kita R 2009 Systematic study of BaSnO<sub>3</sub> doped YBa<sub>2</sub>Cu<sub>3</sub>O<sub>7-x</sub> films *Physica C* **469** 1380–3
  - [12] Varanasi C V, Burke J, Brunke L, Wang H, Lee J H and Barnes P N 2008 Critical current density and microstructure variations in YBa<sub>2</sub>Cu<sub>3</sub>O<sub>7-x</sub> + BaSnO<sub>3</sub> films with different concentrations of BaSnO<sub>3</sub> *J. Mater. Res.* **23** 3363–9
  - [13] Tobita H, Notoh K, Higashikawa K, Inoue M, Kiss T, Kato T, Hirayama T, Yoshizumi M, Izumi T and Shiohara Y 2012 Fabrication of BaHfO<sub>3</sub> doped Gd<sub>1</sub>Ba<sub>2</sub>Cu<sub>3</sub>O<sub>7</sub>-delta coated conductors with the high I-c of 85 A/cm-w under 3 T at liquid nitrogen temperature (77 K) *Supercond. Sci. Technol.* **25** 6
  - [14] Matsushita T et al 2012 Improvement of flux pinning performance at high magnetic fields in GdBa<sub>2</sub>Cu<sub>3</sub>O<sub>y</sub> coated conductors with BHO nano-rods through enhancement of B-c<sub>2</sub> *Supercond. Sci. Technol.* **25** 12
  - [15] Pahlke P et al 2016 Reduced J(c) anisotropy and enhanced in-field performance of thick BaHfO<sub>3</sub>-Doped YBa<sub>2</sub>Cu<sub>3</sub>O<sub>7</sub>-delta films on ABAD-YSZ templates *IEEE Trans. Appl. Supercond.* **26** 3
  - [16] Gautam B, Sebastian M A, Chen S, Haugan T J, Zhang W, Huang J, Wang H and Wu J Z 2018 Microscopic adaptation of BaHfO<sub>3</sub> and Y<sub>2</sub>O<sub>3</sub> artificial pinning centers for strong and isotropic pinning landscape in YBa<sub>2</sub>Cu<sub>3</sub>O<sub>7-x</sub> thin films *Supercond. Sci. Technol.* **31** 025008
  - [17] Gautam B, Sebastian M A, Chen S, Shi J, Haugan T, Xing Z, Zhang W, Huang J, Wang H and Osofsky M 2017 Transformational dynamics of BZO and BHO nanorods imposed by Y<sub>2</sub>O<sub>3</sub> nanoparticles for improved isotropic pinning in YBa<sub>2</sub>Cu<sub>3</sub>O<sub>7-δ</sub> thin films *AIP Adv.* **7** 075308
  - [18] Miura S, Yoshida Y, Ichino Y, Doki Y, Ibi A, Izumi T and Kato T 2016 Flux pinning properties in BaHfO<sub>3</sub>-Doped SmBa<sub>2</sub>Cu<sub>3</sub>O<sub>y</sub> films on metallic substrates fabricated with low temperature growth *IEEE Trans. Appl. Supercond.* **26** 1–5
  - [19] Sebastian M A P, Reichart J N, Ratcliff M M, Bullard T J, Burke J L, Ebbing C R, Panasyuk G Y, Tsai C-F, Zhang W and Huang J 2017 Study of the Flux Pinning Landscape of YBCO thin films with single and mixed phase additions BaMO<sub>3</sub> + Z: m= Hf, Sn, Zr and Z= Y<sub>2</sub>O<sub>3</sub>, Y<sub>211</sub> *IEEE Trans. Appl. Supercond.* **27** 1–5
  - [20] Wang X, Baca F J, Emergo R L, Wu J Z, Haugan T J and Barnes P N 2010 Eliminating thickness dependence of critical current density in YBa<sub>2</sub>Cu<sub>3</sub>O<sub>7-x</sub> films with aligned BaZrO<sub>3</sub> nanorods *J. Appl. Phys.* **108** 3911
  - [21] Petrisor T, Mos R, Nasui M, Gabor M, Augieri A, Celentano G, De Felicis D, Bemporad E, Ciontea L and Petrisor T 2014 The vortex path model analysis of the field angle dependence of the critical current density in nanocomposite YBa<sub>2</sub>Cu<sub>3</sub>O<sub>7-x</sub>-BaZrO<sub>3</sub> films obtained by low fluorine chemical solution deposition *J. Supercond. Novel Magn.* **27** 2493–500
  - [22] Hammerl G, Schmehl A, Schulz R, Goetz B, Bielefeldt H, Schneider C, Hilgenkamp H and Mannhart J 2000 Enhanced supercurrent density in polycrystalline YBa<sub>2</sub>Cu<sub>3</sub>O<sub>7-δ</sub> at 77 K from calcium doping of grain boundaries *Nature* **407** 162
  - [23] Schmehl A, Goetz B, Schulz R, Schneider C, Bielefeldt H, Hilgenkamp H and Mannhart J 1999 Doping-induced enhancement of the critical currents of grain boundaries in YBa<sub>2</sub>Cu<sub>3</sub>O<sub>7-δ</sub> *Europhys. Lett.* **47** 110
  - [24] Horide T, Sakamoto N, Ichinose A, Otsubo K, Kitamura T and Matsumoto K 2016 Hybrid artificial pinning centers of elongated-nanorods and segmented-nanorods in YBa<sub>2</sub>Cu<sub>3</sub>O<sub>7</sub> films *Supercond. Sci. Technol.* **29** 105010
  - [25] Fafard S, Leonard D, Merz J and Petroff P 1994 Selective excitation of the photoluminescence and the energy levels of ultrasmall InGaAs/GaAs quantum dots *Appl. Phys. Lett.* **65** 1388–90
  - [26] Guha S, Madhukar A and Rajkumar K 1990 Onset of incoherency and defect introduction in the initial stages of molecular beam epitaxial growth of highly strained In x Ga<sub>1-x</sub> As on GaAs (100) *Appl. Phys. Lett.* **57** 2110–2
  - [27] Xie Q, Madhukar A, Chen P and Kobayashi N P 1995 Vertically self-organized InAs quantum box islands on GaAs (100) *Phys. Rev. Lett.* **75** 2542
  - [28] Shi J J and Wu J Z 2012 Structural transition of secondary phase oxide nanorods in epitaxial YBa<sub>2</sub>Cu<sub>3</sub>O<sub>7-δ</sub> films on vicinal substrates *Phil. Mag.* **92** 4205–14
  - [29] Shi J J and Wu J Z 2012 Micromechanical model for self-organized secondary phase oxide nanorod arrays in epitaxial YBa<sub>2</sub>Cu<sub>3</sub>O<sub>7-δ</sub> films *Phil. Mag.* **92** 2911–22
  - [30] Shi J J and Wu J Z 2015 Influence of the lattice strain decay on the diameter of self assembled secondary phase nanorod array in epitaxial films *J. Appl. Phys.* **118** 164301
  - [31] Cantoni C, Gao Y, Wee S H, Specht E D, Gazquez J, Meng J, Pennycook S J and Goyal A 2011 Strain-driven oxygen deficiency in self-assembled, nanostructured, composite oxide films *ACS Nano* **5** 4783–9
  - [32] Horide T, Kametani F, Yoshioka S, Kitamura T and Matsumoto K 2017 Structural evolution induced by interfacial lattice mismatch in self-organized YBa<sub>2</sub>Cu<sub>3</sub>O<sub>7-δ</sub> nanocomposite film *ACS Nano* **11** 1780–8
  - [33] Blatter G, Feigel'man M V, Geshkenbein V B, Larkin A I and Vinokur V M 1994 Vortices in high-temperature superconductors *Rev. Mod. Phys.* **66** 1125
  - [34] Gautam B, Sebastian M A, Chen S, Misra S, Huang J, Javier Baca F, Emergo R, Haugan T, Xing Z and Wang H 2018 Probing the effect of interface on vortex pinning efficiency of one-dimensional BaZrO<sub>3</sub> and BaHfO<sub>3</sub> artificial pinning centers in YBa<sub>2</sub>Cu<sub>3</sub>O<sub>7-x</sub> thin films *Appl. Phys. Lett.* **113** 212602
  - [35] Ogunjimi V, Sebastian M A, Zhang D, Gautam B, Jian J, Huang J, Zhang Y, Haugan T J, Wang H and Wu J Z 2021 Enhancing magnetic pinning by BaZrO<sub>3</sub> nanorods forming coherent interface by strain-directed Ca-doping in YBa<sub>2</sub>Cu<sub>3</sub>O<sub>7-x</sub> nanocomposite films *Supercond. Sci. Technol.* **34** 104002
  - [36] Baca F J, Barnes P N, Emergo R L S, Haugan T J, Reichart J N and Wu J Z 2009 Control of BaZrO<sub>3</sub> nanorod alignment in YBa<sub>2</sub>Cu<sub>3</sub>O<sub>7-x</sub> thin films by microstructural modulation *Appl. Phys. Lett.* **94** 3
  - [37] Sebastian M A, Gautam B, Ebbing C R, Panasyuk G Y, Susner M A, Huang J, Zhang W, Wang H, Wu J Z and Haugan T J 2019 Comparison study of the flux pinning enhancement of YBa<sub>2</sub>Cu<sub>3</sub>O<sub>7-δ</sub> thin films with BaHfO<sub>3</sub> + Y<sub>2</sub>O<sub>3</sub> single- and mixed-phase additions *IEEE Trans. Appl. Supercond.* **29** 8002005
  - [38] Chen S, Sebastian M, Gautam B, Wilt J, Haugan T, Xing Z and Wu J 2017 Enhancement of isotropic pinning force in YBCO films with BaZrO<sub>3</sub> nanorods and Y<sub>2</sub>O<sub>3</sub> nanoparticles *IEEE Trans. Appl. Supercond.* **27** 1–5
  - [39] Gautam B, Sebastian M A, Chen S, Haugan T J, Zhang W, Huang J, Wang H and Wu J Z 2017 Microscopic adaptation of BaHfO<sub>3</sub> and Y<sub>2</sub>O<sub>3</sub> artificial pinning centers for strong

- and isotropic pinning landscape in  $\text{YBa}_2\text{Cu}_3\text{O}_{7-x}$  thin films *Supercond. Sci. Technol.* **31** 025008
- [40] Emergo R L S, Baca F J, Wu J Z, Haugan T J and Barnes P N 2010 The effect of thickness and substrate tilt on the BZO splay and superconducting properties of  $\text{YBa}_2\text{Cu}_3\text{O}_{7-\delta}$  films *Supercond. Sci. Technol.* **23** 115010
- [41] Civale L, Maiorov B, MacManus-Driscoll J, Wang H, Holesinger T, Foltyn S, Serquis A and Arendt P 2005 Identification of intrinsic ab-plane pinning in  $\text{YBa}_2\text{Cu}_3\text{O}_7$  thin films and coated conductors *IEEE Trans. Appl. Supercond.* **15** 2808–11
- [42] Klenov D O and Stemmer S 2006 Contributions to the contrast in experimental high-angle annular dark-field images *Ultramicroscopy* **106** 889–901
- [43] Zhang W, Chen A, Jian J, Zhu Y, Chen L, Lu P, Jia Q, MacManus-Driscoll J L, Zhang X and Wang H 2015 Strong perpendicular exchange bias in epitaxial  $\text{La}_{0.7}\text{Sr}_{0.3}\text{MnO}_3$ :  $\text{biFeO}_3$  nanocomposite films through vertical interfacial coupling *Nanoscale* **7** 13808–15
- [44] Scholtz J, Van Eenige E, Wijngaarden R and Griessen R 1992 Pressure dependence of  $T_c$  and  $H_{c2}$  of  $\text{YBa}_2\text{Cu}_4\text{O}_8$  *Phys. Rev. B* **45** 3077
- [45] Khan M Z, Rivasto E, Tikkanen J, Rijckaert H, Malmivirta M, Liedke M O, Butterling M, Wagner A, Huhtinen H and Van Driessche I 2019 Enhanced flux pinning isotropy by tuned nanosized defect network in superconducting  $\text{YBa}_2\text{Cu}_3\text{O}_{6+x}$  films *Sci. Rep.* **9** 1–12
- [46] Samoilenov S, Boytsova O, Amelichev V and Kaul A 2011 Anisotropic strain of  $\text{BaZrO}_3$ ,  $\text{BaCeO}_3$  and  $\text{Y}_2\text{O}_3$  nanoinclusions in a  $\text{YBa}_2\text{Cu}_3\text{O}_{7-x}$  epitaxial film matrix and its relation to the oxygen content of the superconductor *Supercond. Sci. Technol.* **24** 055003
- [47] Wu J et al 2019 Pinning efficiency of one-dimensional artificial pinning centers in  $\text{YBa}_2\text{Cu}_3\text{O}_{7-x}$  thin films *IEEE Trans. Appl. Supercond.* **29** 1–5
- [48] Goyal A, Kang S, Leonard K J, Martin P M, Gapud A A, Varela M, Paranthaman M, Ijaduola A O, Specht E D and Thompson J R 2005 Irradiation-free, columnar defects comprised of self-assembled nanodots and nanorods resulting in strongly enhanced flux-pinning in  $\text{YBa}_2\text{Cu}_3\text{O}_{7-\delta}$  films *Supercond. Sci. Technol.* **18** 1533
- [49] Gutierrez J et al 2007 Strong isotropic flux pinning in solution-derived  $\text{YBa}_2\text{Cu}_3\text{O}_{7-x}$  nanocomposite superconductor films *Nat. Mater.* **6** 367–73
- [50] Horide T, Nagao S, Izutsu R, Ishimaru M, Kita R and Matsumoto K 2018 Geometric and compositional factors on critical current density in  $\text{YBa}_2\text{Cu}_3\text{O}_{7-\delta}$  films containing nanorods *Supercond. Sci. Technol.* **31** 065012
- [51] Chen S, Sebastian M A, Gautam B, Wilt J, Chen Y, Sun L, Xing Z, Haugan T and Wu J 2017 Generating mixed morphology  $\text{BaZrO}_3$  artificial pinning centers for strong and isotropic pinning in  $\text{BaZrO}_3$ – $\text{Y}_2\text{O}_3$  double-doped YBCO thin films *Supercond. Sci. Technol.* **30** 125011
- [52] Wu J and Shi J 2017 Interactive modeling-synthesis-characterization approach towards controllable *in situ* self-assembly of artificial pinning centers in RE-123 films *Supercond. Sci. Technol.* **30** 103002
- [53] Obradors X and Puig T 2014 Coated conductors for power applications: materials challenges *Supercond. Sci. Technol.* **27** 044003
- [54] Malmivirta M, Rijckaert H, Paasonen V, Huhtinen H, Hynninen T, Jha R, Awana V S, Van Driessche I and Paturi P 2017 Enhanced flux pinning in YBCO multilayer films with BCO nanodots and segmented BZO nanorods *Sci. Rep.* **7** 1–8
- [55] Ogunjimi V, Gautam B, Sebastian M A, Haugan T and Wu J 2019 The angular range of effective pinning by one-dimensional artificial pinning centers in  $\text{BaZrO}_3/\text{YBa}_2\text{Cu}_3\text{O}_{7-x}$  nanocomposite films *AIP Adv.* **9** 085110
- [56] Ogunjimi V, Gautam B, Sebastian M A, Haugan T and Wu J 2020 The effect of APC/YBCO interface on the angular range of effective pinning by one-dimensional artificial pinning centers in  $\text{YBa}_2\text{Cu}_3\text{O}_{7-x}$  nanocomposite films *IOP Conf. Ser.: Mater. Sci. Eng.* **756** 012025
- [57] Wu J, Gautam B and Ogunjimi V 2020 Pinning efficiency of artificial pinning centers in superconductor nanocomposite films *Superconductivity* (Berlin: Springer) p 29
- [58] Klie R F, Buban J P, Varela M, Franceschetti A, Jooss C, Zhu Y, Browning N D, Pantelides S T and Pennycook S J 2005 Enhanced current transport at grain boundaries in high- $T_c$  superconductors *Nature* **435** 475–8
- [59] Askeland D R, Phulé P P, Wright W J and Bhattacharya D 2003 The science and engineering of materials **6th Edition**
- [60] Richerson D W and Lee W E 2018 *Modern Ceramic Engineering: Properties, Processing, and Use in Design* (Boca Raton, FL: CRC Press)
- [61] Sharma V, Kumar P, Dev P and Pilania G 2020 Machine learning substitutional defect formation energies in  $\text{ABO}_3$  perovskites *J. Appl. Phys.* **128** 034902
- [62] Horide T, Ishimaru M and Matsumoto K 2019 Observation of inhomogeneous depinning in  $\text{YBa}_2\text{Cu}_3\text{O}_7$  composite multilayers *Supercond. Sci. Technol.* **32** 085001
- [63] Ichinose A, Naoe K, Horide T, Matsumoto K, Kita R, Mukaida M, Yoshida Y and Horii S 2007 Microstructures and critical current densities of YBCO films containing structure-controlled  $\text{BaZrO}_3$  nanorods *Supercond. Sci. Technol.* **20** 1144